Inorganic Chemistry

Article

pubs.acs.org/IC

Terms of Use

A Cubic Fe_4Mo_4 Oxo Framework and Its Reversible Four-Electron Redox Chemistry

Jan P. Falkenhagen,[†] Beatrice Braun,[†] Eckhard Bill,[‡] Dominik Sattler,[§] and Christian Limberg*[,†]

[†]Institut für Chemie, Humboldt-Universität zu Berlin, Brook-Taylor-Straße 2, 12489 Berlin, Germany

[‡]Max Planck Institute for Chemical Energy Conversion (formerly Bioinorganic Chemistry), Stiftstraße 34−36, 45470 Mülheim, Germany

[§]Institut für Chemie und Biochemie, Freie Universität Berlin, Takustraße 3, 14193 Berlin, Germany

Supporting Information

ABSTRACT: The potential of iron molybdates as catalysts in the Formox process stimulates research on aggregated but molecular iron−molybdenum oxo compounds. In this context, $[(Me_3TACN)Fe](OTf)_2$ was reacted with $(nBu_4N)_2[MoO_4]$, which led to an oxo cluster, $[[(Me_3TACN)Fe][\mu\text{-}(MoO_4\text{-}\kappa^3O,O',O'')]]_4$ (**1**, Fe_4Mo_4) with a distorted cubic structure, where the corners are occupied by $(Me_3TACN)Fe^{2+}$ and $[Mo{=}O]^{4+}$ units in an alternating fashion, being bridged by oxido ligands. The cyclic voltammogram revealed four reversible oxidation waves that are assigned to four consecutive $Fe^{II} \rightarrow Fe^{III}$ transfers and motivated attempts to isolate compounds containing the respective cations. Indeed, a salt with a $Fe^{II}_2Fe^{III}_2Mo^{VI}_4$ constellation, $[Fe_4Mo_4](TCNQ)_2$ (**2**), could be isolated after treatment with TCNQ. The $Fe^{II}Fe^{III}_3Mo^{VI}_4$ stage could be reached via oxidation with DDQ or 3 equiv of thianthrenium hexafluorophosphate ($ThPF_6$), giving $[Fe_4Mo_4](DDQ)_3$ (**4**) or $[Fe_4Mo_4](PF_6)_3$ (**5**), respectively. The fully oxidized $Fe^{III}_4Mo^{VI}_4$ state was generated through oxidation with 4 equiv of $ThPF_6$, leading to $[Fe_4Mo_4](PF_6)_4$, which showed a unique behavior: upon storage, one of the $[Mo{=}O]^{4+}$ corners inverts, so that the terminal oxido ligand is located in the interior of the cage, leading to the formation of $[[(Me_3TACN)Fe]_4[\mu\text{-}([MoO_4]_3[MoO_4(MeCN\text{-}\kappa N)])\text{-}\kappa^3O,O',O'')](PF_6)_4$ (**7**). In this form, the compound could no longer be employed to enter the cyclic voltammogram recorded for **1**, **3**, and **5** from the oxidized side; no discrete redox events were observed. Compounds **1**−**3** and **7** were characterized structurally and **1**, **3**, and **7** additionally by SQUID measurements and Mössbauer spectroscopy. The data reveal a high degree of charge delocalization. $^{16}O/^{18}O$ exchange experiments with labeled water performed with **1** revealed an interesting parallel with the Formox catalyst: water−^{18}O exchanges its label with all of the oxido ligands (bridging and terminal). This property relates to the ion mobility being held responsible for the activity of iron molybdate catalysts compared to neat MoO_3 or Fe_2O_3.

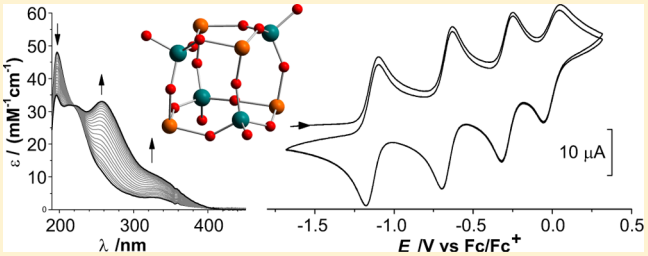

INTRODUCTION

In recent years, we have been interested in molecular heterobimetallic oxo compounds that can mimic certain surface structural units of corresponding heterogeneous catalysts composed of two metal oxide components.[1−6] The fact that $Fe_2(MoO_4)_3$ catalysts are employed for the oxidation of methanol to formaldehyde in the so-called Formox process has now spurred us to aim at aggregated but molecular Fe−O−Mo compounds. While some purely inorganic polyoxometal aggregates[7−15] and coordination polymers[12,16−22] featuring Fe−O−Mo entities have been published, until 2013 only five structurally characterized molecular coordination compounds have been reported where molybdate units are bridging iron ions,[13,23−28] ligated, for instance, by the tris(2-pyridylmethyl)-amine (TPA) ligand. Recently, we have extended this field to iron complexes being connected to organomolybdate units via oxido ligands, and these proved to be efficient initiators for autoxidation reactions.[29] Also, in these investigations, the tetradentate TPA ligand had been chosen as a coligand at iron, leaving two coordination sites vacant at the iron center for interaction with the organomolybdate.[29] To increase the connectivity within the Fe−O−Mo framework, we then decided to replace TPA by tridentate 1,4,7-trimethyl-1,4,7-triazacyclononane (Me_3TACN) and to return to molybdate without organic ligands. This led to a cubic $Fe^{II}_4Mo^{VI}_4$ compound, $[[(Me_3TACN)Fe][\mu\text{-}(MoO_4\text{-}\kappa^3O,O',O'')]]_4$ (**1**), exhibiting a remarkable reversible redox chemistry.

RESULTS AND DISCUSSION

Synthesis and Properties of $[[(Me_3TACN)Fe][\mu\text{-}(MoO_4\text{-}\kappa^3O,O',O'')]]_4$ [1]. $[[(Me_3TACN)Fe](OTf)_2$ was prepared from iron(II) triflate $[Fe(OTf)_2]$ and Me_3TACN via a published procedure.[30] Reaction with equimolar amounts of $(nBu_4N)_2[MoO_4]$ led to the complex **1** (Fe_4Mo_4) in a yield of 85% (Scheme 1).

Received: March 19, 2014
Published: July 1, 2014

 © 2014 American Chemical Society dx.doi.org/10.1021/ic500584a | Inorg. Chem. 2014, 53, 7294−7308

Scheme 1. Synthesis of 1

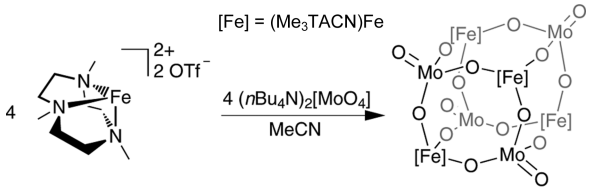

Its molecular structure, as determined by single-crystal X-ray diffraction, is shown in Figure 1. It consists of a distorted cubic arrangement in which each of the four $(Me_3TACN)Fe^{2+}$ moieties is connected to three of four $[Mo{=}O]^{4+}$ units via oxido ligands, resulting in distorted octahedral coordination spheres at the iron and distorted tetrahedral coordination spheres at the molybdenum centers.

The $[Mo{=}O]^{4+}$ units are characterized by Mo−O distances between 1.732(2) and 1.749(2) Å, consistent with elongated Mo=O bonds. The distances between the molydenum atoms and the bridging oxido ligands are in the range of shortened Mo−O single bonds [range of 1.758(2)−1.792(2) Å]. The fact that per molybdenum center the differences in the Mo−O bond lengths between the shortest and longest bonds are relatively small suggests a certain amount of delocalization. As expected, the observed O=Mo−O angles are very similar, ranging from 106.71(10) to 107.81(11)°; the variation among the O−Mo−O angles is only slightly larger [110.44(10)−112.51(10)°]. In contrast, both values of the O−Fe−O angles, ranging from 88.9(9) to 103.63(9)°, and the Mo−O−Fe angles [123.48(11)−159.55(14)°] are very heterogeneous and illustrate the flexibility of the core structure.

he ^{1}H NMR spectrum of **1** dissolved in dichloromethane-d_2 at 20 °C displays three broad signals at 101.8 (6H, $\Delta\nu_{1/2}$ = 290 Hz), 42.4 (9H, $\Delta\nu_{1/2}$ = 180 Hz), and 40.5 (6H, $\Delta\nu_{1/2}$ = 630 Hz) ppm, indicating an effective 3-fold symmetry and thus a fluxional behavior in solution, which by rapid interconversion of the $\lambda\lambda\lambda$ and $\delta\delta\delta$ isomers of the Me_3TACN ligands on the time scale of the NMR experiment gives rise to distinct signals for syn and anti protons of the CH_2 groups, respectively.[31]

In high-resolution electrospray ionization mass spectrometry (HR-ESI-MS) experiments of **1**, dissolved in either methanol or acetonitrile and employing mild ionization conditions, the molecular ions $\mathbf{1}^+$ (calcd m/z 1547.977; found m/z 1547.974) and $\mathbf{1}^{2+}$ (calcd m/z 773.988; found m/z 773.989) are observed as the main signals (Figure S2A in the Supporting Information, SI). No shifts were observed when **1** was sprayed from a solution in methanol-d_4, verifying that the charge for both ions stems from the removal of one or two electrons rather than the binding of additional protons. Under harsher ionization conditions (Figure S2B in the SI), a consecutive loss of up to three neutral Me_3TACN ligands can be observed, while at the same time, the core cluster remains intact, giving rise to additional signals corresponding to $[\mathbf{1} - (Me_3TACN)]^+$ (calcd m/z 1376.803; found m/z 1376.793), $[\mathbf{1} - (Me_3TACN)_2]^+$ (calcd m/z 1205.629; found m/z 1205.621), and $[\mathbf{1} - (Me_3TACN)_3]^+$ (calcd m/z 1034.455; found m/z 1034.448).

The same fragments are observed in an infrared multiphoton dissociation (IRMPD) experiment with mass-selected $\mathbf{1}^+$ ions (Figure S2C in the SI). This confirms that the signals additionally observed under harsher ionization conditions are indeed fragments generated from intact $\mathbf{1}^+$ ions and shows the cluster core to be highly stable in the gas phase. Interestingly, a maximum of three rather than four Me_3TACN ligands are lost even at highest laser flux density and longer irradiation times. This is consistent with the ionization mode: A one-electron oxidation during electrospray ionization leads to $Fe^{II}_3Fe^{III}Mo^{VI}_4$, and ligand loss is apparently much easier from the iron(II) centers, while the ligand is more strongly bound at Fe^{III}.

Mass spectrometry (MS) can also be used to monitor an exchange of ^{16}O versus ^{18}O with water present in solution. The $^{16}O/^{18}O$ exchange reaction of **1** in an acetonitrile solution containing 50 equiv of water−^{18}O (91%) per oxygen atom in **1** at room temperature proceeds within 2 days, as indicated by a clear mass shift (Figure 2). The most abundant isotope peak shifted by 28 amu, indicating that, on average, 14 of 16 oxygen atoms have been exchanged, which is consistent with a simulation of purely statistical exchange considering the amount and purity of water−^{18}O used. This reaction has also been studied in the gas phase. The reaction of $\mathbf{1}^+$ ions with water−^{18}O in the high vacuum of the instrument's accumulation hexapole (pressure ca. 1.0×10^{-4} mbar) has been monitored for reaction times of up to 2000 s (Figure 2A). Given the observed reaction rate in solution at room temperature, these reaction delays are certainly too short

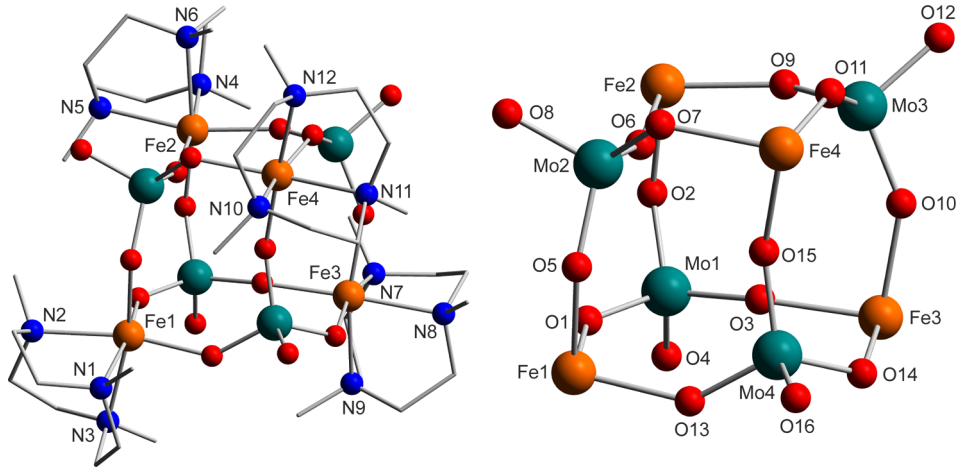

Figure 1. Molecular structure and atom-labeling scheme of $\mathbf{1}\cdot(MeCN)_5$. Hydrogen atoms and cocrystallized solvent molecules have been omitted for clarity. For selected bond lengths and angles, see Tables 3 and 4.

dx.doi.org/10.1021/ic500584a | Inorg. Chem. 2014, 53, 7294−7308

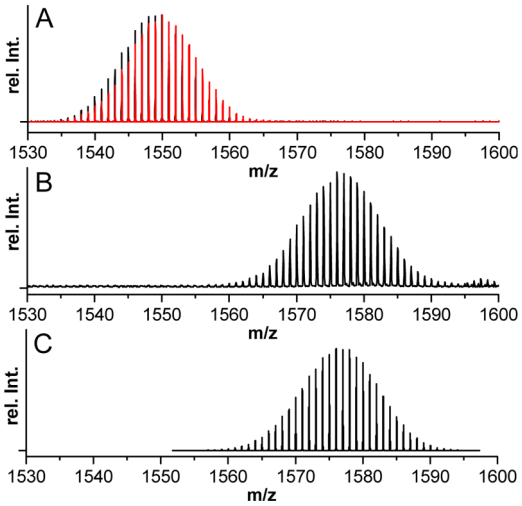

Figure 2. $^{16}O/^{18}O$ isotope exchange experiments with water−^{18}O: (A) isotope pattern before any isotope exchange (—) and isotope pattern after 2000 s of exchange reaction in the gas phase (red —); (B) isotope pattern of a sample that has undergone a 2 day $^{16}O/^{18}O$ exchange reaction with 50 equiv of water−^{18}O (91%) in acetonitrile; (C) simulation of statistical isotope exchange based on the known $^{16}O/^{18}O$ contents in the water employed and in **1**.

to expect large isotope pattern shifts. Nevertheless, the small shift observed qualitatively demonstrates that $^{16}O/^{18}O$ exchange occurs in the gas phase as well.

An investigation of **1** in acetonitrile by cyclic voltammetry revealed four reversible redox events with half-wave potentials at −1.135, −0.661, −0.284, and −0.005 V vs Fc/Fc^+. Reversibility becomes obvious through characteristic differences (ΔE) between the cathodic (E_{pc}) and anodic (E_{pa}) peak potentials between 65 and 100 mV and through the fact that the cyclic voltammogram does not change over the course of more than 10 cycles (Figure 3).

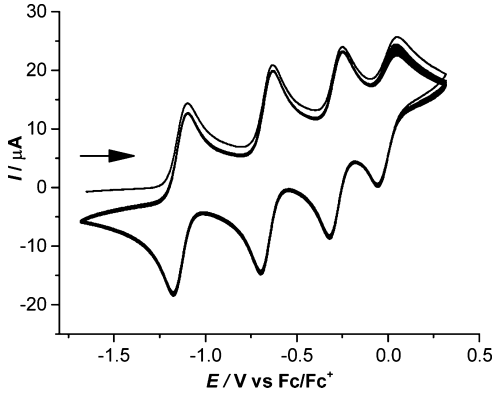

Figure 3. Cyclic voltammogram of **1** (0.001 M acetonitrile and 0.1 M TBAP) at 200 mV/s (10 cycles): Four reversible redox events are observed at −0.005 V (ΔE_p = 100 mV), −0.284 V (ΔE_p = 71 mV), −0.661 V (ΔE_p = 65 mV), and −1.135 V (ΔE_p = 77 mV) vs Fc/Fc^+.

To examine whether it is possible to quantitatively oxidize and reduce **1** in a series of sequential one-electron oxidation/reduction steps, with the core cluster remaining intact, a spectroelectrochemical experiment was carried out. Therefore, **1** was dissolved in acetonitrile, and a cyclic voltammetry experiment was conducted at 5 mV/s cycling between −1.6 and 0.4 V (vs Fc/Fc^+), which was followed by UV/vis spectroscopy.

Indeed, over the course of the experiment, cyclic changes in the UV/vis spectrum with only a minimal change of the intensity are observed. The most intense absorption band at 200 nm decreases, and a new band at 270 nm with a shoulder at 350 nm appears (Figure 4A), as clearly becomes visible in the calculated difference spectrum (Figure 4B).

This suggested that a stepwise oxidation of **1** on synthetic scales might be possible, and this was pursued by employing various oxidation agents. For the selection of suitable oxidants, the half-wave potentials and the number of atoms to be oxidized had to be considered. Moreover, the Nernst equation for reversible electron-transfer processes requires an oxidant to have a redox potential that is 0.236 V more positive to achieve 99% conversion to the oxidized product. Hence, tetracyanoquinodimethane (TCNQ), 2,3-dichloro-5,6-dicyano-1,4-benzoquinone (DDQ), and thianthrenium hexafluorophosphate ($ThPF_6$) were chosen as reagents for the stepwise oxidation of **1**.

Independent Synthesis of Salts of the Oxidized Cations. *Reaction of 1 with TCNQ.* While all attempts to isolate a salt containing the singly oxidized $Fe^{II}_3Fe^{III}Mo^{VI}_4$ core failed, the oxidation of two iron centers could be achieved using TCNQ, which, dissolved in acetonitrile, has a redox potential of −0.30 V (vs Fc/Fc^+).[32]

Treatment of an acetonitrile solution of **1** with 2 equiv of TCNQ (Scheme 2) led to a green solution, from which blue single crystals of $[[(Me_3TACN)Fe][\mu\text{-}(MoO_4\text{-}\kappa^3O,O',O'')]]_4(TCNQ)_2(MeCN)$ [**2**·(MeCN)] could be grown (Figure 5). The unit cell contains two conserved Fe_4Mo_4 entities, each of which is surrounded by two TCNQ units being arranged in pairs through π stacking with a face-to-face alignment. Each pair consists of one TCNQ unit and its symmetry-equivalent partner. The distances between the planes defined by the six-membered rings amount to 2.962(2) Å for the first pair and 3.054(2) Å for the second pair, which is well below the sum of the van der Waals radii.[33] Two distinct types of pairs can be identified, differing from each other in their orientation within the unit cell and in the positioning of the respective molecules to each other. The TCNQ pairs in the center of the unit cell exhibit a "slipped" conformation, where the two molecules are shifted against each other by 2.19 Å along and 0.30 Å perpendicularly to the main axis. Within the second type of pairs, the molecules are shifted along the main axis by 0.19 Å and perpendicularly by about 1.29 Å.[34]

A comparison of the Fe_4Mo_4 core of **2**·(MeCN) (Table 3) with the core of the parent cluster **1**·$(MeCN)_5$ shows significant contractions of all Fe−N bond lengths. A similar behavior is observed with regard to the Mo═O bonds, which are considerably shorter, namely, in the range of 1.689(4)−1.712(4) Å. Despite a general contraction also of the Fe−O bond lengths, opposing trends are observed with regard to the specific iron centers. While Fe1−O and Fe4−O bonds are in the range of 2.037(4)−2.122(4) Å, the Fe2−O and Fe3−O bonds are considerably shorter, showing values from 1.890(4) to 1.970(4) Å. The Mo−O single bond lengths show only minor differences compared to those in **1**·$(MeCN)_5$; the average bond length is nearly unaffected by oxidation (Table 3). It is informative to also compare the metric data of the TCNQ units to those of the neutral, unperturbed molecules: TCNQ can act as a one-electron acceptor, as envisaged, but also as a two-electron and even a three-electron acceptor, and each electron added leads to characteristic changes[35,36] within the TCNQ

dx.doi.org/10.1021/ic500584a | Inorg. Chem. 2014, 53, 7294−7308

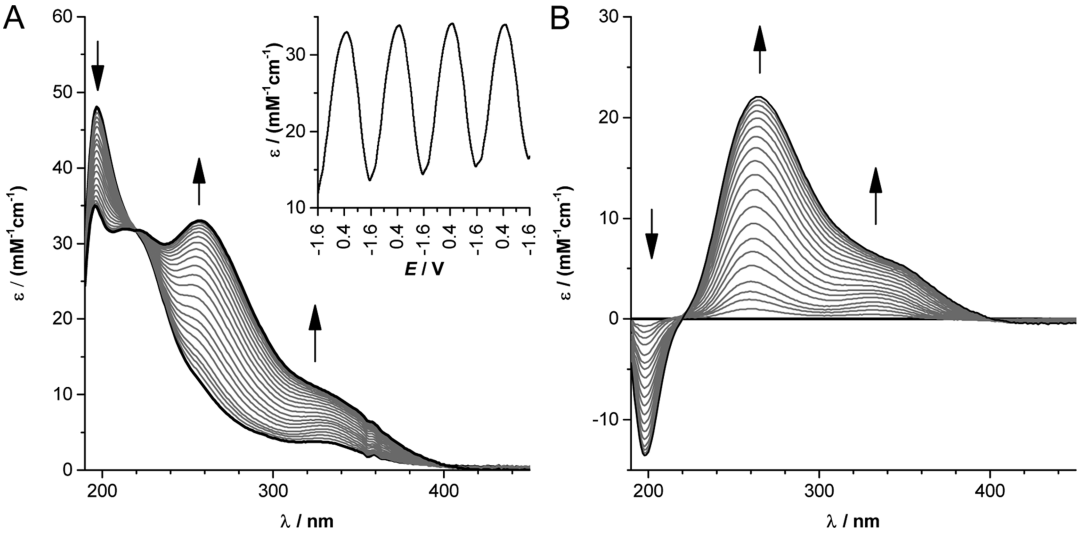

Figure 4. (A) Spectral changes in the UV/vis region during electrochemical oxidation of a solution of **1** (0.1 mM) and TBAP (0.1 M) in acetonitrile at a scan rate of 5 mV/s in the range from −1.6 to 0.4 V vs Fc/Fc^+ (inset: ϵ at 257 nm vs applied potential during four consecutive oxidation/reduction cycles). (B) Difference plot. The UV/vis spectrum of the solution measured at −1.6 V was subtracted from each spectrum.

Scheme 2. Synthesis of 2 and 3 by Oxidation of 1 with TCNQ and Subsequent Anion Exchange Using $[n\mathrm{Bu_4N}](\mathrm{PF_6})$

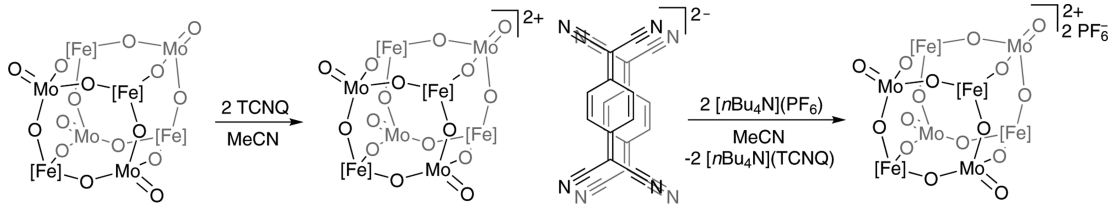

1 **2** **3**

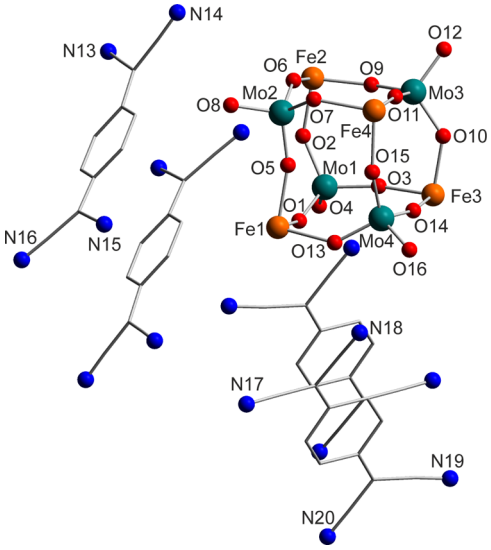

Figure 5. Molecular structure and atom-labeling scheme of the cation of **2**·(MeCN) surrounded by two TCNQ units. To visualize the π-stacking interactions, two additional TCNQ units (unlabeled) are shown, which are symmetry-equivalent to the labeled TCNQ units. Me_3TACN ligands, hydrogen atoms, and cocrystallized solvent molecules have been omitted for clarity. For selected bond lengths and angles, see Tables 3 and 4.

framework. Thus, its structural analysis can help to elucidate the charge of the TCNQ units and, in turn, the charge of the Fe_4Mo_4 core. In comparison with the structure of the neutral TCNQ molecule, the entities within the structure of **2**·(MeCN) exhibit elongated exo- and endocyclic C═C double bonds, which can be explained by a partial occupation of the π^* orbitals. The structural data of the TCNQ units within **2**·(MeCN) favorably agree with those published in the literature for $TCNQ^{\bullet-}$ and $[(TCNQ)_2]^{2-}$ [see the table for a detailed comparison of TCNQ metrics within **2**·(MeCN) and literature data].[35,37−39] Hence, on this basis, the presence of $[(TCNQ)_2]^-$ anions or solely cocrystallized neutral TCNQ molecules can be excluded.

The same conclusions can be derived from the results of UV/vis spectroscopic investigations. A UV/vis spectrum of **2** recorded for an acetonitrile solution shows three main $TCNQ^{n-}$ related absorption maxima at wavelengths of 421, 743, and 843 nm. Further bands are observed at 409, 666, 680, 743, 761, and 824 nm (Figure 6). Analysis of the difference spectrum determined by subtraction of the spectrum of **1** reveals extinction coefficients of $\epsilon/\mathrm{M^{-1}cm^{-1}}$ (λ_{max}/nm) = 24300 (421), 22100 (743), and 41300 (843) in accordance with reported values of 24300 (420) and 43300 (842) for the $TCNQ^{\bullet-}$ radical anion.[40] Further valuable information for identification of the species present in solution can be derived from determination of the absorption ratio of the bands at 421 and 843 nm, A_{421}/A_{843}. A ratio between 0.5 and 0.6 points to a radical anion with the presence of neutral TCNQ leads to a value >0.5; for instance, a $[(TCNQ)_2]^{\bullet-}$ pair leads to a ratio of 2.[40] For **2**, a mean value of 0.59 is determined, which further supports the presence of a radical anion. IR spectroscopy is an additional valuable tool in this context because also the ν(CN), ν(C═C), and ν(C−C)

dx.doi.org/10.1021/ic500584a | Inorg. Chem. 2014, 53, 7294−7308

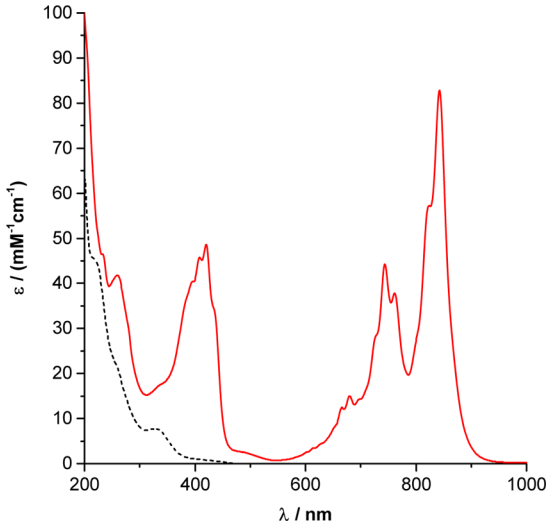

Figure 6. UV/vis spectra of **2** (red —) dissolved in acetonitrile [0.87×10^{-5} M, 2 mm path length; $TCNQ^{\bullet-}$ absorption maxima λ_{max}, nm (ϵ, M^{-1} cm^{-1}) at 421 (24300), 743 (22100), and 843 (41300)] and **1** (- - -). ϵ was calculated relative to the concentration of **1** (compare Figure 9).

absorptions are sensitive to the charge state of the TCNQ unit. For **2**, characteristic bands at 2177, 2151, 1586, and 1503 cm^{-1} are observed. A comparison with literature values again corroborates the presence of $TCNQ^{\bullet-}$ radical anions (Table 1) as well as the absence of dimers incorporating neutral TCNQ.

Finally, an electron paramagnetic resonance (EPR) spectrum recorded for a solution of **2** in acetonitrile after cooling to 77 K showed a signal with a g value of 2.002, characteristic for the $TCNQ^{\bullet-}$ radical. While a radical concentration of only 2.0% was determined via double integration against a standard with a known concentration of TEMPO, this is what should be expected if $TCNQ^{\bullet-}$ radical anions form $[(TCNQ)_2]^{2-}$ dimers upon cooling,[35,44−46] as in fact found in the solid-state structure of **2**·(MeCN) (vide supra). All of these results together show that the crystals grown for **2**·(MeCN) exclusively contain $TCNQ^{\bullet-}$ radical anions, and thus the Fe_4Mo_4 units carry two positive charges. Accordingly, repeated dissolution of **2** in acetonitrile, reaction with 2 equiv of $[nBu_4N](PF_6)$, and precipitation by the addition of diethyl ether afforded after drying under high vacuum $[[(Me_3TACN)Fe][\mu\text{-}(MoO_4\text{-}\kappa^3O,O',O'')]]_4(PF_6)_2$ (**3**) as a brown solid. Single crystals of **3**·$(MeCN)_{0.25}$ suitable for X-ray diffraction analysis were grown by layering a solution of acetonitrile with diethyl ether (Figure S1 in the SI). Upon comparison of the structural features of **3**·$(MeCN)_{0.25}$ with those of **2**·(MeCN), as expected it is found that both molecular structures appear to be relatively similar. The Fe_4Mo_4 core structure is conserved, and the differences in Fe−N as well as Mo=O and Mo−O bond lengths are negligible. Interestingly, in contrast to the molecular structure of **2**·(MeCN), in the structure of **3**·$(MeCN)_{0.25}$, only one of the four iron atoms exhibits distinctly shorter Fe−O bonds of 1.930(3)−1.9359(19) Å compared to those of the others; two of the remaining iron atoms are characterized by Fe−O distances of 1.971(2)−2.046(2) Å and the fourth by distances between 2.019(2) and 2.0875(18) Å.

*Reaction of **1** with DDQ.* Targeting the oxidation of three iron atoms within **1**, it was reacted with DDQ (Scheme 3), which has a redox potential of 0.013 V (vs Fc/Fc^+) in an acetonitrile solution,[32] to give a blackberry-colored solution. Subsequent removal of all volatiles under reduced pressure afforded $[Fe_4Mo_4](DDQ)_3$ (**4**) as a red-brown solid. Like TCNQ, DDQ can also act as a multielectron acceptor, so that again a comparison of the spectroscopic data of **4** with the literature data on DDQ species was required to unequivocally determine the charge of the Fe_4Mo_4 entity.

A useful probe is the ν_{CN} band observed at 2234 cm^{-1} for neutral DDQ. A reduction leads to a bathochromic shift, and the extent reveals information on the number of electrons transferred. The shift of $\Delta\tilde{\nu}$ = 24 cm^{-1} observed here compares well with shifts reported in the literature for the $DDQ^{\bullet-}$ radical anion (2217 cm^{-1}; see Table 2). The characteristic band corresponding to the aromatic C=C stretching vibration at 1578 cm^{-1} (lit.: 1580 cm^{-1}) matches well also. Thus, from the IR spectroscopic measurements, the formation of DDQ^{2-} can be excluded.[47]

To determine the number of $DDQ^{\bullet-}$ equivalents formed, an excess of DDQ was added to a solution of **1** in acetonitrile, and the change in the UV/vis spectrum was analyzed. The reaction leads to the immediate appearance of characteristic bands at 456, 549, and 588 nm, indicating the formation of $DDQ^{\bullet-}$ (Figure 7), and per molecule the formation of 3 equiv of $DDQ^{\bullet-}$ is observed (ϵ_{588} = 6300 M^{-1} cm^{-1}).[47] Hence, the Fe_4Mo_4 cluster carries three positive charges; that is, three iron centers are in the oxidation state III+, and one iron atom is in the oxidation state II + ($Fe^{II}Fe^{III}{}_3Mo^{VI}{}_4$). Unfortunately, attempts to crystallize **4** were not successful because of decomposition of the $DDQ^{\bullet-}$ radicals when dissolved in dioxane, diethyl ether, or tetrahydrofuran and the lack of suitable alternative methods.

Reaction with $ThPF_6$. Targeting the oxidation of all iron atoms within **1**, it was reacted with 4 equiv of $ThPF_6$ (Scheme 4), which has a redox potential of 0.86 V (vs Fc/Fc^+) in an acetonitrile solution,[32] to yield $[[(Me_3TACN)Fe][\mu\text{-}(MoO_4\text{-}\kappa^3O,O',O'')]]_4(PF_6)_4$ (**6**). Layering a concentrated solution of **6** in acetonitrile with diethyl ether afforded single crystals that could be subjected to X-ray diffraction analysis.

Remarkably, this led to the structure of $[[(Me_3TACN)Fe]_4\mu\text{-}([MoO_4]_3[MoO_4(MeCN\text{-}\kappa N)])\text{-}\kappa^3O,O',O'')](PF_6)_4(MeCN)_4$ [**7**·$(MeCN)_4$] (Figure 8), an isomer of **6**, whose core structure differs from those in **1**·$(MeCN)_5$, **2**·(MeCN), and **3**·$(MeCN)_{0.25}$. In **7**·$(MeCN)_4$, the two Mo=O units around Mo1 and Mo3 are statically disordered, and the groups of atoms belonging to either of the two split positions are labeled A or B, respectively. In each cation, one $MoO_4{}^{2-}$ unit is inverted, that is, the Mo=O function (Mo1A or Mo3B) points toward the inside of the cluster. The oxygen atoms of these Mo=O functions show contact with the three remaining molybdenum ions at distances between 2.846(2) and 2.929(2) Å, well below the sum of the van der

Table 1. Comparison of Vibrational Data for $[(TCNQ)_n]^{m-}$ Species and 2

$TCNQ$[36,40−42]	$TCNQ^-$ [36,40−42]	$[(TCNQ)_2]^{-}$[43]	$TCNQ^{2-}$ [36,42]	$TCNQ^{3-}$ [36]	**2**
2222−2228	2181−2198	2190	2164	2035	2177
	2153−2174	2160	2096	1901	2151
1545	1578−1590	1565	1598	1577	1586
1540	1504−1505	1508	1503	1476	1503

dx.doi.org/10.1021/ic500584a | Inorg. Chem. 2014, 53, 7294−7308

Scheme 3. Synthesis of 4 and 5 by Oxidation of 1 with 3 equiv of DDQ or $ThPF_6$ and Subsequent Crystallization of 5 To Give a Mixture of $3\cdot(MeCN)_{0.25}$ and $7\cdot(MeCN)_4$

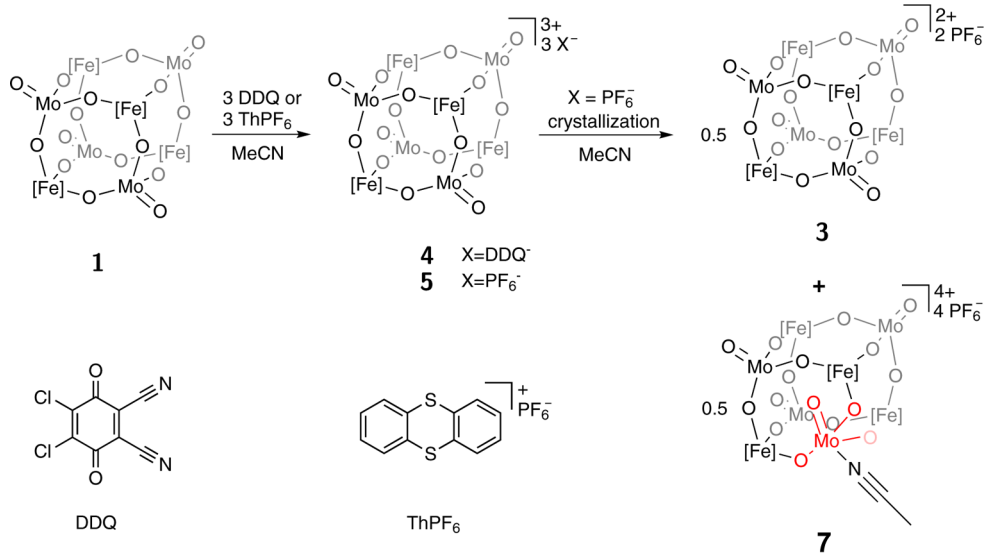

Table 2. Vibrational Data of $(DDQH_x)^{n-}$ and 4[47]

	DDQ	DDQ^{-} [a]	$DDQH^{-}$ [b]	DDQ^{2-} [b]	$DDQH_2$	4
ν(OH)			3553 m		3295 br, s	
ν(CN)	2234 w	2217 s	2243 s	2187 m	2257	2210 m
	2246 w			2200 s	2269	
ν(C=O)	1691 s					
	1701 s					
ν(C=C)	1550 w		1675 s	1618 w		1540–1574
ν(C=C) (aromatic)		1580 s	1460 s	1457 s	1575 m	
					1465 s	

[a] $n-Et_4N^+$ salt. [b] Na^+ salt.

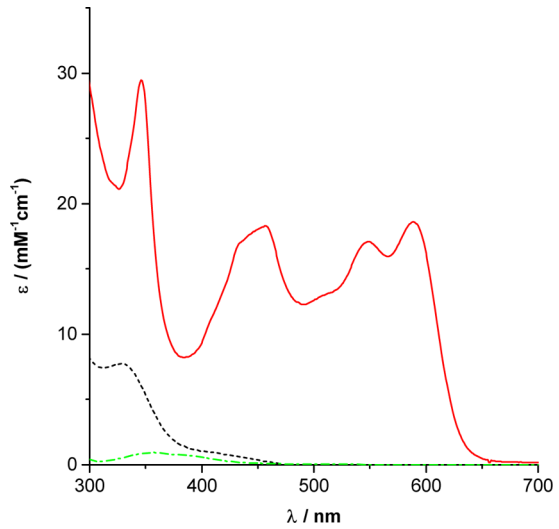

Figure 7. UV/vis spectra of **1** (- - -), **1**/DDQ (exc.) (red —), and DDQ (green –·–). ϵ was calculated relative to the concentration of **1** (compare Figure 9).

Waals radii.[33] Moreover, the Mo1A and Mo3B ions are coordinated by an additional molecule of acetonitrile with a long Mo···N distance of 2.488(3) Å, resulting in distorted trigonal-bipyramidal coordination spheres around Mo1A and Mo3B (τ = 1.04),[48] respectively, and elongated Mo=O bonds Mo1A/Mo3B 1.732(2)/1.715(3) Å (Tables 3 and 4). All Fe–N bonds are considerably shorter than the corresponding bonds in any of the Fe_4Mo_4 and $Fe_4Mo^{2+}{}_4$ complexes ranging from 2.1611(16) to 2.1896(17) Å. Also, most of the Fe–O bonds are significantly shorter [1.9411(12)–1.9616(12) Å] than those in the related clusters, with the exception of the very short Fe1–O bonds in $3\cdot(MeCN)_{0.25}$. The Mo=O and Mo–O bond lengths follow trends observed earlier. While the former are shorter compared to $1\cdot(MeCN)_5$, $2\cdot(MeCN)$, and $3\cdot(MeCN)_{0.25}$ (with the exception of Mo1A/Mo3B=O, vide supra), the latter show slightly higher values [1.7617(12)–1.8598(13) Å].

Employing only 3 equiv of $ThPF_6$ for the oxidation of **1** permits isolation of a second salt featuring the $Fe^{II}Fe^{III}{}_3Mo^{VI}{}_4$ core, namely, $[[(Me_3TACN)Fe][\mu\text{-}(MoO_4\text{-}\kappa^3O,O',O'')]]_4(DDQ)_3$ (**5**), where the $DDQ^{\bullet-}$ anions of **4** are replaced by PF_6^- anions. Interestingly, attempts to grow crystals suitable for single-crystal X-ray diffraction starting from isolated **5** resulted in the parallel formation of single crystals of $3\cdot(MeCN)_{0.25}$ and the $Fe^{III}{}_4Mo^{VI}{}_4$ compound $7\cdot(MeCN)_4$ (as an acetonitrile solvate), indicating a disproportionation reaction during crystallization.

UV/vis Spectroscopy. In a comparison of the UV/vis spectra of the pure and isolated compounds **1**, **3**, and **7** (Figure 9), it was found that new bands at 270 and 350 nm [which may be assigned to oxo → Fe^{III} and amine → Fe^{III} charge-transfer (CT) transitions, respectively][49,50] arise concomitantly to stepwise cluster oxidation, while the intensity of the absorption at 220 nm

dx.doi.org/10.1021/ic500584a | Inorg. Chem. 2014, 53, 7294–7308

Scheme 4. Synthesis of 6 by Oxidation of 1 with 4 equiv of $ThPF_6$ and 7·$(MeCN)_4$ by Subsequent Crystallization

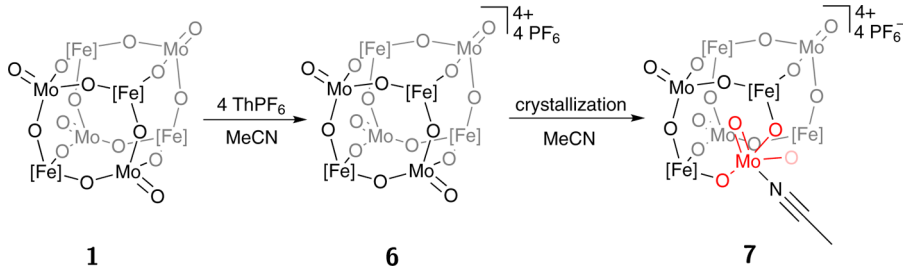

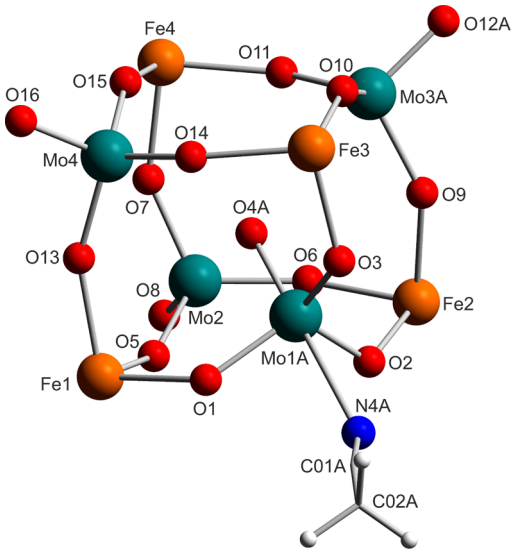

Figure 8. Molecular structure and atom-labeling scheme of the cation of 7·$(MeCN)_4$, with split position A and Me_3TACN ligands. Hydrogen atoms (except for those of the coordinating MeCN ligand) and cocrystallized solvent molecules have been omitted for clarity. For selected bond lengths and angles, see Tables 3 and 4.

(oxo → Mo^{VI} CT transition)[51] decreases (Figure 9A). This behavior becomes even more apparent when depicted in a difference spectrum calculated from the spectra of **7** and **1** (Figure 9B).

These spectral changes favorably agree with those observed during the spectroelectrochemical experiments (Figure 4), confirming that the same reaction is monitored in both cases.

Cyclic Voltammetry. As described earlier, a cyclic voltammetry investigation of **1** in acetonitrile had revealed that **1** can be oxidized in a sequence of four one-electron oxidation steps. In comparison, the cyclic voltammogram recorded for **2** dissolved in the same solvent (Figure 10) can be understood as a superposition of the voltammograms of the two precursor compounds **1** and TCNQ, which show only minimal shifts. This suggests that their reaction is a pure electron-transfer reaction. Moreover, the measured open-circuit potential E_{oc} = −0.343 V, used as the initial voltage, can be used as an indicator that the core structure is stable in a $Fe^{II}_2Fe^{III}_2Mo^{VI}_4$ state. Further proof can be derived from measurements on **3** (Figure 11A). Here, an unchanged cyclic voltammogram (without a superimposed cyclic voltammogram as the anion is not redox active) with redox events at −1.132 (ΔE_p = 76 mV), −0.658 (ΔE_p = 70 mV), −0.280 (ΔE_p = 77 mV), and −0.016 (ΔE_p = 98 mV) V vs Fc/Fc^+ is observed, which is in very good agreement with that of **1**. Again, the open-circuit potential E_{oc} = −0.364 V reflects the oxidation states of the cluster core iron ions, that is, $Fe^{II}_2Fe^{III}_2Mo^{VI}_4$.

Cyclic voltammograms observed for **4**, like in the case of **2**, appear as superpositions of those of the precursor compounds. To record cyclic voltammograms without the DDQ related redox events, **5** (featuring the same cation as **4**) was studied after in situ generation from **3** using 1 equiv of $ThPF_6$ (vide supra). With signals at −1.132 (ΔE_p = 75 mV), −0.661 (ΔE_p = 71 mV), −0.280 (ΔE_p = 73 mV), and −0.008 (ΔE_p = 90 mV) V, the cyclic voltammogram (Figure 11B) is essentially identical with those of **1** and **3**. Again, the measured open-circuit potential of E_{oc} = −0.132 V reflects the charge state of the core cluster ion.

Although the open-circuit potential at E_{oc} = 0.019 V measured for a solution of pure **7** in acetonitrile agrees with a $Fe^{III}_4Mo^{VI}_4$ oxidation state of **7**, no distinct redox events are observed if redissolved single crystals of **7** are investigated by cyclic voltammetry. However, when **1** or isolated **3** is treated with 4/2 equiv of $ThPF_6$ in situ to yield **6**, the cyclic voltammogram typical of **1** or **3** is observed showing a sequence of four redox events, albeit displaying minor shifts (Figure 11C): Signals are observed at −1.132 (67 mV), −0.660 (72 mV), −0.284 (75 mV), and −0.018 (95 mV) V. Because the cyclic voltammetry does not change over days, we ascribe this different behavior of in situ prepared **6** versus isolated **7** to the structural reorganization taking place during crystallization: Apparently, the inversion of one of the molybdate units is a slow process and, once it has occurred, as in the case of **7**, prohibits reversible redox events. In summary, the results of the cyclic voltammetry measurements confirm the stability of the core cluster throughout the reaction; the cyclic voltammograms recorded for compounds in the $Fe^{II}_4Mo^{VI}_4$, $Fe^{II}_2Fe^{III}_2Mo^{VI}_4$, $Fe^{II}Fe^{III}_3Mo^{VI}_4$, and $Fe^{III}_4Mo^{VI}_4$ states differ only slightly because they are all accessible independent from the starting point (Figures 3 and 11).

Mössbauer and Magnetic Measurements (SQUID). Mössbauer and SQUID measurements were performed to study the electronic structure of iron in the isolated compounds. The zero-field Mössbauer spectrum of **1** recorded at 80 K shows a doublet with broad resonance bands (Figure 12), the antisymmetric intensity distributions of which indicate distinct heterogeneity of the iron sites. The spectrum can be well simulated with four symmetric quadrupole doublets of equal intensity and with virtually identical isomer shifts, δ = 1.17(1) mm/s, but with distinctly different quadrupole splitting in the range ΔE_Q = 1.20−2.60 mm/s. The high isomer shifts are characteristic and unique for high-spin iron(II) complexes. Their similarity reflects bonding situations with the same overall covalence and average bond lengths.

In contrast, the differences in the quadrupole splitting reveal variances in the charge asymmetry at the four iron sites of **1**, resulting from axial and rhombic distortions of the coordination polyhedra. The moderate strength of the quadrupole splitting is

dx.doi.org/10.1021/ic500584a | Inorg. Chem. 2014, 53, 7294−7308

Table 3. Selected Bond Lengths for 1·(MeCN)$_5$, 2·(MeCN), 3·(MeCN)$_{0.25}$, and 7·(MeCN)$_4$

		1·(MeCN)$_5$	2·(MeCN)	3·(MeCN)$_{0.25}$	7·(MeCN)$_4$A	7·(MeCN)$_4$B
Fe−N	Fe1−N1	2.279(3)	2.224(4)	2.212(2)	2.1765(15)	
	Fe1−N2	2.266(2)	2.252(4)	2.217(2)	2.1768(15)	
	Fe1−N3	2.272(3)	2.219(4)	2.220(2)	2.1717(15)	
	Fe2−N4	2.241(3)	2.203(4)	2.218(3)	2.1890(14)	
	Fe2−N5	2.267(2)	2.216(4)	2.229(3)	2.1861(16)	
	Fe2−N6	2.273(3)	2.219(4)	2.240(2)	2.1653(16)	
	Fe3−N7	2.257(3)	2.211(4)	2.213(3)	2.1828(14)	
	Fe3−N8	2.258(3)	2.213(5)	2.219(3)	2.1638(16)	
	Fe3−N9	2.276(3)	2.234(4)	2.221(2)	2.1611(16)	
	Fe4−N10	2.268(3)	2.226(4)	2.228(2)	2.1770(15)	
	Fe4−N11	2.290(2)	2.242(5)	2.220(2)	2.1806(16)	
	Fe4−N12	2.255(3)	2.229(4)	2.195(2)	2.1896(17)	
Fe−O	Fe1−O1	2.054(2)	2.122(4)	1.930(3)	1.9411(12)	
	Fe1−O5	2.065(2)	2.055(4)	1.9359(19)	1.9526(13)	
	Fe1−O13	2.025(2)	2.080(4)	1.931(2)	1.9553(13)	
	Fe2−O2	2.085(2)	1.942(3)	2.0875(18)	1.9600(13)	
	Fe2−O6	2.045(2)	1.899(4)	2.019(2)	1.9455(11)	
	Fe2−O9	2.069(2)	1.948(4)	2.023(2)	1.9491(12)	
	Fe3−O3	2.056(2)	1.961(4)	2.018(2)	1.9526(12)	
	Fe3−O10	2.036(2)	1.970(4)	2.001(2)	1.9421(12)	
	Fe3−O14	2.067(2)	1.890(4)	2.046(2)	1.9616(12)	
	Fe4−O7	2.078(2)	2.051(4)	2.0207(19)	1.9427(13)	
	Fe4−O11	2.045(2)	2.104(4)	1.971(2)	1.9447(11)	
	Fe4−O15	2.051(2)	2.037(4)	1.990(2)	1.9559(13)	
Mo═O	Mo1−O4	1.738(2)	1.710(3)	1.7044(19)	1.732(2)	1.682(3)
	Mo2−O8	1.743(2)	1.701(4)	1.697(2)	1.6933(12)	
	Mo3−O12	1.749(2)	1.689(4)	1.708(2)	1.651(2)	1.715(3)
	Mo4−O16	1.732(2)	1.712(4)	1.693(2)	1.6918(13)	
Mo−O	Mo1−O1	1.779(2)	1.740(4)	1.819(3)	1.7894(12)	1.8080(12)
	Mo1−O2	1.781(2)	1.800(3)	1.7589(17)	1.7679(13)	1.8598(13)
	Mo1−O3	1.766(2)	1.783(4)	1.722(2)	1.7959(12)	1.7961(12)
	Mo2−O5	1.778(2)	1.755(4)	1.7985(18)	1.7829(12)	
	Mo2−O6	1.758(2)	1.810(4)	1.752(2)	1.7886(11)	
	Mo2−O7	1.792(2)	1.767(3)	1.7752(19)	1.7820(12)	
	Mo3−O9	1.769(2)	1.799(4)	1.763(2)	1.8300(12)	1.7682(12)
	Mo3−O10	1.775(2)	1.783(4)	1.7876(19)	1.8031(12)	1.7888(13)
	Mo3−O11	1.778(2)	1.725(4)	1.782(2)	1.7937(11)	1.7617(12)
	Mo4−O13	1.781(2)	1.758(4)	1.794(2)	1.7812(12)	
	Mo4−O14	1.785(2)	1.804(4)	1.752(2)	1.7832(12)	
	Mo4−O15	1.768(2)	1.733(4)	1.7739(19)	1.7902(12)	

typical of quasi-trigonal TACN complexes. For comparison, the dinuclear $[(TACN)_2Fe^{II}{}_2Cl_3]^+$ cation was reported to show δ = 1.16 mm/s and ΔE_Q = 2.79 mm/s at 77 K in an acetonitrile solution, whereas the corresponding BPh_4^- salt has ΔE_Q scattered between 0.92 and 1.86 mm/s.[52] Applied-field Mössbauer measurements yielded a negative sign for those quadrupole splittings in that case and, hence, of the corresponding electric-field-gradient (efg) tensors. This rendered the ground-state orbital of iron(II) in $[(TACN)_2Fe^{II}{}_2Cl_3]^+$ to be of the d_{z^2} type (i.e., a low-lying a_1 orbital determines the valence contribution to the efg). According to the similarity of δ and ΔE_Q, we may assume a similar a_1-determined ground state of iron(II) in **1**, where three oxido ligands complement the TACN coordination moiety. In both cases, symmetry-dependent mixing with excited 1e/2e orbitals and covalency seems to reduce ΔE_Q to the observed values around 2 mm/s instead of the ca. 4 mm/s expected for a pure d_{z^2} ground-state orbital.[53]

The semioxidized complex 3·(MeCN)$_{0.25}$ measured at 80 K shows, in addition to the pattern of ferrous iron, a second Mössbauer subspectrum with lower isomer shift and weak quadrupole splitting, which is typical of high-spin iron(III) in general (Figure 13). A fit with two Lorentzian doublets yielded δ = 1.18 mm/s and ΔE_Q = 2.26 mm/s for the ferrous part and δ = 0.47 mm/s and ΔE_Q = 0.31 mm/s for the ferric part; the isomer shift of the latter, in particular, matches those of other iron(III) TACN complexes.[54] The 1:1 intensity ratio of the subspectra reveals the presence of a mixed-valence $Fe^{II}{}_2Fe^{III}{}_2Mo^{VI}{}_4$ core for **3**, for which both the ferrous and ferric sites are indistinguishable.

The Mössbauer spectrum of the oxidized compound **7** shows a single doublet with δ = 0.43 mm/s and ΔE_Q = 0.49 mm/s at 80 K (Figure 14). The large line width of the spectrum (ca. 1 mm/s) presumably results from intermediate paramagnetic relaxation of the local spins $S_i = {}^5/_2$. At 160 and 240 K, it correspondingly reduces, on average, to 0.76 and 0.59 mm/s, respectively (Figures S3 and S4 in the SI). The Mössbauer parameters corroborate the all-ferric character of **7**, presenting a $Fe^{III}{}_4Mo^{VI}{}_4$ core.

Magnetization measurements of the all-ferrous, mixed-valent, and all-ferric complexes 1·(MeCN)$_5$, 3·(MeCN)$_{0.25}$, and 7·

dx.doi.org/10.1021/ic500584a | Inorg. Chem. 2014, 53, 7294−7308

Table 4. Selected Angles for 1·(MeCN)$_5$, 2·(MeCN), 3·(MeCN)$_{025}$, and 7·(MeCN)$_4$

		1·MeCN)$_5$	2·(MeCN)	3·(MeCN)$_{0.25}$	7·(MeCN)$_4$A	7·(MeCN)$_4$B
Mo−O−Fe	Mo1−O1−Fe1	138.34(12)	142.9(2)	152.69(15)	124.02(7)	152.00(7)
	Mo1−O2−Fe2	127.23(11)	145.9(2)	131.86(9)	123.29(7)	149.40(7)
	Mo1−O3−Fe3	159.55(14)	163.5(2)	168.06(15)	128.36(6)	154.29(7)
	Mo2−O5−Fe1	139.72(12)	162.9(2)	145.76(11)	147.61(7)	
	Mo2−O6−Fe2	158.69(14)	146.9(2)	169.25(13)	150.77(7)	
	Mo2−O7−Fe4	123.69(12)	135.30(18)	138.47(11)	147.91(7)	
	Mo3−O9−Fe2	146.73(13)	151.3(3)	158.22(15)	148.05(7)	123.66(6)
	Mo3−O10−Fe3	147.46(12)	137.7(2)	145.45(11)	150.67(7)	124.22(6)
	Mo3−O11−Fe4	144.88(12)	172.9(3)	145.96(12)	152.09(7)	127.91(7)
	Mo4−O13−Fe1	137.82(12)	139.0(2)	145.21(13)	154.51(7)	
	Mo4−O14−Fe3	123.48(11)	163.8(3)	139.68(11)	151.30(7)	
	Mo4−O15−Fe4	152.09(12)	160.3(3)	168.38(12)	148.25(7)	
O−Fe−O	O1−Fe1−O5	95.73(8)	88.63(15)	98.90(9)	94.80(5)	
	O1−Fe1−O13	97.16(8)	96.75(16)	99.68(10)	93.45(5)	
	O5−Fe1−O13	95.84(8)	92.18(15)	97.95(9)	96.57(5)	
	O2−Fe2−O6	90.15(9)	97.89(15)	92.14(8)	95.55(5)	
	O2−Fe2−O9	100.46(9)	95.84(15)	95.16(9)	94.68(5)	
	O6−Fe2−O9	92.24(9)	97.20(18)	90.67(9)	95.64(5)	
	O3−Fe3−O10	93.79(9)	95.72(15)	91.28(9)	94.81(5)	
	O3−Fe3−O14	91.02(8)	96.79(18)	88.83(9)	94.56(5)	
	O10−Fe3−O14	100.34(9)	96.96(18)	96.32(8)	94.70(5)	
	O7−Fe4−O11	103.63(9)	92.17(16)	97.51(8)	94.32(5)	
	O7−Fe4−O15	88.90(8)	95.01(15)	92.31(8)	95.50(5)	
	O11−Fe4−O15	91.02(9)	90.68(19)	93.00(8)	95.96(5)	
O−Mo═O	O1−Mo1−O4	107.81(11)	107.62(19)	107.06(10)	102.49(7)	102.76(10)
	O2−Mo1−O4	107.57(11)	108.71(17)	109.92(8)	104.52(8)	113.60(10)
	O3−Mo1−O4	107.55(11)	107.55(19)	108.76(10)	101.40(8)	105.15(10)
	O5−Mo2−O8	106.71(10)	107.91(19)	109.59(10)	105.11(6)	
	O6−Mo2−O8	107.35(10)	107.73(19)	106.63(10)	105.71(6)	
	O7−Mo2−O8	107.22(10)	110.75(17)	109.17(10)	105.56(6)	
	O9−Mo3−O12	107.72(10)	108.2(2)	105.39(11)	104.17(9)	103.82(11)
	O10−Mo3−O12	107.71(10)	109.0(2)	107.70(10)	106.11(9)	102.54(11)
	O11−Mo3−O12	107.54(11)	108.1(2)	109.07(10)	110.09(8)	100.87(10)
	O13−Mo4−O16	107.27(10)	110.08(19)	108.79(11)	105.22(6)	
	O14−Mo4−O16	107.69(10)	105.8(2)	107.37(11)	105.99(6)	
	O15−Mo4−O16	107.06(11)	108.2(2)	108.17(10)	106.43(6)	
O−Mo−O	O1−Mo1−O2	111.80(10)	111.39(16)	110.21(10)	115.30(6)	110.03(6)
	O1−Mo1−O3	111.46(10)	110.57(18)	110.03(11)	114.13(6)	113.22(6)
	O2−Mo1−O3	110.44(10)	110.86(16)	110.77(10)	116.25(5)	111.74(6)
	O5−Mo2−O6	112.51(10)	109.79(17)	109.10(9)	112.18(5)	
	O5−Mo2−O7	112.00(9)	110.63(16)	111.75(8)	112.62(6)	
	O6−Mo2−O7	110.71(10)	109.96(17)	110.47(9)	114.69(5)	
	O9−Mo3−O10	111.28(10)	109.75(17)	112.90(10)	111.23(5)	114.90(6)
	O9−Mo3−O11	111.03(10)	111.0(2)	110.92(11)	111.76(5)	116.40(6)
	O10−Mo3−O11	111.35(10)	110.8(2)	110.62(9)	112.95(5)	115.24(6)
	O13−Mo4−O14	111.46(10)	110.4(2)	111.68(10)	113.87(6)	
	O13−Mo4−O15	112.28(9)	110.93(18)	109.50(10)	112.56(6)	
	O14−Mo4−O15	110.81(10)	111.2(2)	111.22(9)	112.01(6)	

(MeCN)$_4$, respectively, revealed very weak spin coupling of the paramagnetic metal ions in the cubane structures (Figures 15 and 16). The effective magnetic moments above 100−200 K are temperature-independent and very close to the values expected for four noninteracting local spins $S = 2$ and/or $S = {}^5/_2$. Below this regime, the values decline because of the combined effects of field saturation, single-ion zero-field splitting, and eventually very weak antiferromagnetic spin coupling. The minor variation of the data did not allow us to readily disentangle the different influences and the many parameters. The fits presented in Figures 15 and 16 therefore are not necessarily unique, but they yield upper limits for the strengths of the exchange coupling constants, which all are found to be on the order ±0.1 cm^{-1}. The very weak coupling is not unexpected because extended diamagnetic −O═Mo−O− units bridge the paramagnetic iron centers.

COMPARISON OF THE MOLECULAR Fe_4Mo_4 OXO CLUSTERS WITH THE $Fe_2(MoO_4)_3$ CATALYSTS

There are still controversial discussions on the nature of the active sites and the functioning of the iron(III) molybdates employed as catalysts in the Formox process, in particular also

dx.doi.org/10.1021/ic500584a | Inorg. Chem. 2014, 53, 7294−7308

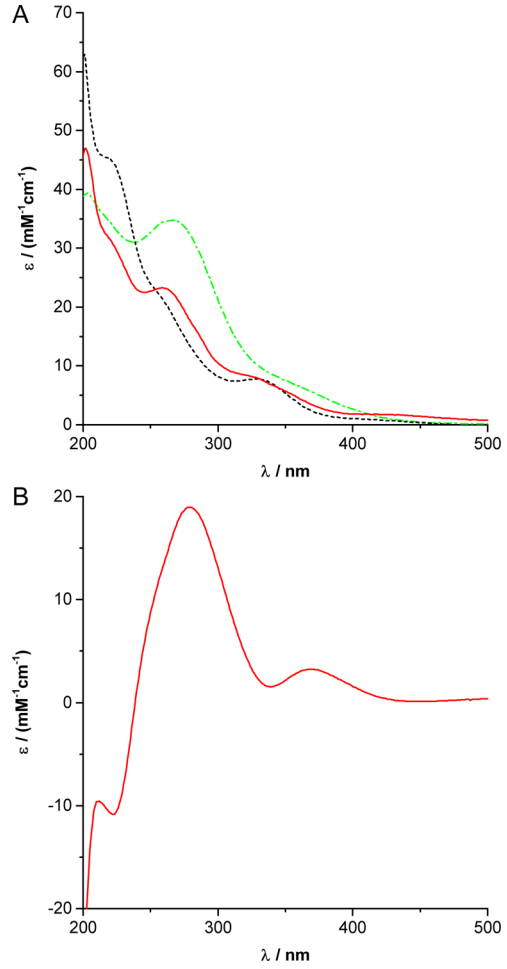

Figure 9. (A) UV/vis spectra of **1** (- - -), **3** (red —), and **7** (green —). (B) Difference spectrum of the spectra of **7** and **1** in acetonitrile.

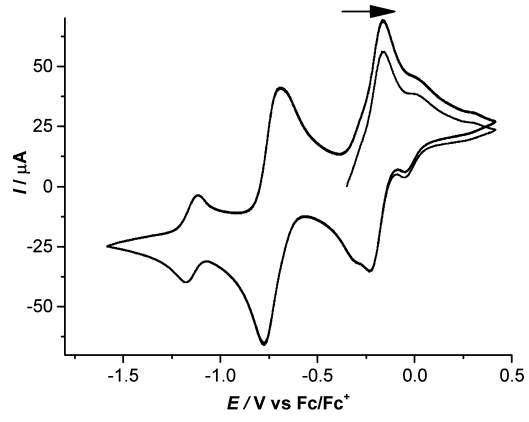

Figure 10. Cyclic voltammetry measurement on a solution of 0.1 M TBAP and 1 mM **2** in MeCN at 100 mV/s and 25 °C.

with regard to the role of iron. According to the view prevailing today, methanol oxidation proceeds at oxido molybdenum moieties; whether these are mono-, di-, or trinuclear with molybdenum atoms featuring one or two terminal oxido ligands remains a matter of debate.[55−65] Recently, $[Mo{=}O]^{4+}$ units bound to the oxo surface have again been put forward in this context.[66] Complexes **6** and **7** contain Mo═O units in an environment of oxido ligands linked to three iron(III) centers. However, perhaps because of the Me_3TACN ligands, which shield the iron centers and thus enable isolation of such molecules, the oxidation potential is surprisingly low and the compounds are not capable of oxidizing methanol (keep in mind though that the Formox catalyst acts at 270−400 °C, so that a functional comparison is difficult).[67] It is interesting to note though that electrons added to the all-ferric form **6** (finally) reduce the iron centers. It has been shown that one role of iron as part of the $Fe_2(MoO_4)_3$ catalysts is the enhancement of the anion mobility, by which they facilitate retention of the oxidized state at the surface. This has been supported by passing water−^{18}O over the surfaces of MoO_3 and $Fe_2(MoO_4)_3$ at 300 °C: While no exchange was observed in the case of MoO_3, $Fe_2(MoO_4)_3$ exchanged lattice oxygen.[68] It is interesting to see that oxido ligands are also mobile in a molecular model like **1**.

CONCLUSIONS

The reaction of $[(Me_3TACN)Fe](OTf)_2$ with $(nBu_4N)_2[MoO_4]$ yields an electronically and structurally unique system composed of four $(Me_3TACN)Fe^{2+}$ moieties and four $[Mo{=}O]^{4+}$ units, which are linked via oxido ligands to give a distorted cubic framework. This oxo cluster shows four reversible oxidation waves in cyclic voltammetry experiments that transfer the iron(II) ions successively into the oxidation state III+, and three of the resulting cations ($Fe^{II}_2Fe^{III}_2Mo^{VI}_4$, $Fe^{II}Fe^{III}_3Mo^{VI}_4$, and $Fe^{III}_4Mo^{VI}_4$) could also be generated independently via chemical oxidations. These led to isolable salts that could be fully characterized and structurally investigated, revealing a high degree of charge delocalization. Their cyclic voltammograms match the one of the parent all-iron(II) precursor, which illustrates reversibility independently of the cations present. However, the all-iron(III) product is not indefinitely stable as such and undergoes an unprecedented rearrangement: One of the $[Mo{=}O]^{4+}$ corners of the distorted cube experiences an inversion, so that the respective terminal oxido ligand is placed in the interior of the cage. After that, the typical cyclic voltammogram is no longer observed, and electrochemical reductions become irreversible. The all-ferrous form exchanges all of its oxygen atoms with water, proving high anion mobility, which is similar to the behavior observed for industrially relevant ferric molybdates. Currently, we are investigating the potential of the compounds as redox reagents in contact with hydrocarbons and their further oxidation via oxygen-atom transfer.

EXPERIMENTAL SECTION

General Procedures. All manipulations were carried out in a glovebox or else by means of Schlenk-type techniques involving the use of a dry argon atmosphere. The NMR spectra were recorded on a Bruker DPX 300 NMR spectrometer (^1H 300.1 MHz) at 23 °C. Chemical shifts are reported in ppm, relative to the residual proton signal of dichloromethane-d_2 at 5.32 ppm. Microanalyses were performed on a Hekatech Euro EA 3000 elemental analyzer. IR spectra were recorded using samples prepared as KBr pellets with a Shimadzu FTIR-8400S spectrometer. UV/vis data were recorded on an Agilent 8453A diode-array spectrometer using quartz cuvettes.

Electrochemical Measurements. *Cyclic Voltammetry.* Measurements were performed in a custom-made jacketed small-volume electrochemical cell under an inert-gas atmosphere at 25 °C using a GAMRY Reference 600 potentiostat. The three-electrode setup consisted of ALS 3 mm platinum disk working, Radiometer M241Pt counter, and platinum wire pseudoreference or Ag/Ag^+ [0.01 M $AgNO_3$ and 0.1 M tetrabutylammonium hexafluorophosphate (TBAP) in MeCN] reference electrodes. Measurements were carried out on 1 mM solutions of the analyte employing 0.1 M solutions of the supporting electrolyte (TBAP) in the respective solvent. In all experiments, the uncompensated resistance R_u was measured at the

dx.doi.org/10.1021/ic500584a | Inorg. Chem. 2014, 53, 7294−7308

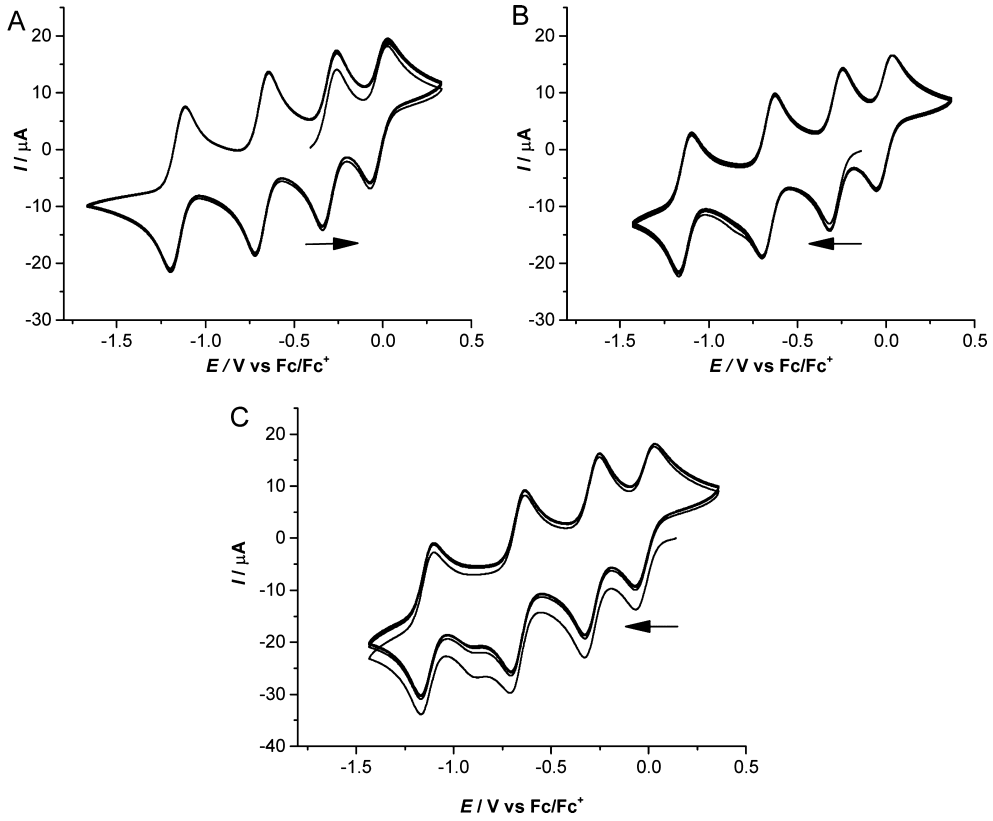

Figure 11. Cyclic voltammograms of (A) **3** (0.001 M in acetonitrile and 0.1 M TBAP) at 100 mV/s (10 cycles), (B) **3** reacted with 1 equiv of $ThPF_6$ (0.001 M in acetonitrile and 0.1 M TBAP) at 100 mV/s, and (C) **3** reacted with 2 equiv of $ThPF_6$ (0.001 M in acetonitrile and 0.1 M TBAP) at 200 mV/s. The irreversible reduction observed at −0.960 V stems from an $ThPF_6$ impurity, which could not be removed.

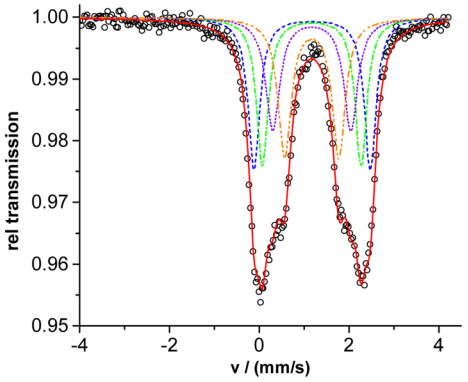

Figure 12. Mössbauer spectrum of **1** recorded at 80 K. The red line represents a fit with four Lorentzian quadrupole doublets of equal intensity and isomer shifts δ = 1.17 mm/s. Quadrupole splittings are ΔE_Q = 1.28, 1.73, 2.20, and 2.60 mm/s, and line widths (full width at half-maximum, fwhm) = 0.35, 0.39, 0.31, and 0.31 mm/s (dotted lines, inner to outer subspectra). Alternatively, a similar fit is possible without discriminating the outer two doublets; i.e., three subspectra are used with the intensity ratio 1:1:2, and δ = 1.18 mm/s, ΔE_Q = 2.43 mm/s, and fwhm = 0.43 mm/s for the outer subspectrum accounting for two iron sites.

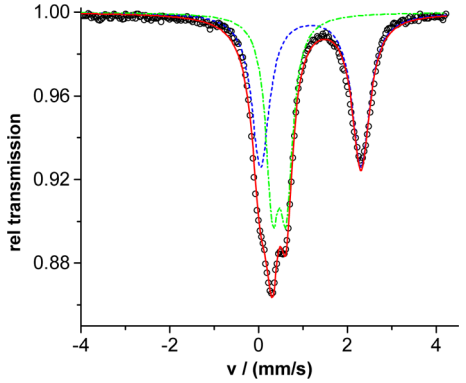

Figure 13. Mössbauer spectrum of **3**·$(MeCN)_{0.25}$ recorded at 80 K. The lines represent a fit with two Lorentzian doublets (see the text).

open-circuit potential (E_{oc}), and positive feedback *iR* compensation was used to compensate for this effect. At the end of each experiment, a small amount of ferrocene was added to the respective solution, and all data were then referenced against the Fc/Fc^+ redox couple as an internal standard.

Spectroelectrochemistry. Spectroelectrochemistry was performed similarly employing a modified BASi 1 mm thin-layer quartz-glass spectroelectrochemical cell with platinum gauze working, platinum wire counter, and Ag/Ag^+ (0.01 M $AgNO_3$ and 0.1 M TBAP in MeCN) reference electrodes. The measurements were carried out in a temperature-controlled environment using a Unispeks USP-203-A cryostat.

Crystal Structure Determination. Single-crystal data for **3**·$(MeCN)_{0.25}$ were collected with a Bruker D8 Venture diffractometer using Cu Kα radiation (λ = 1.54178 Å). Data for **1**·$(MeCN)_5$, **2**·(MeCN), and **7**·$(MeCN)_4$ were collected with a STOE IPDS 2T diffractometer using Mo Kα radiation (λ = 0.71073 Å). The radiation sources were an Incoatec microsource with a multilayer optics monochromator for **3**·$(MeCN)_{0.25}$ and a sealed tube generator with a graphite monochromator for the other complexes. In all cases, crystals were mounted on glass fibers, then transferred into the cold nitrogen gas stream of the diffractometer, and measured at 100(2) K. The structures were solved by direct methods (*SHELXS-2013*) and refined by full-matrix least-squares procedures based on F^2 with all measured

dx.doi.org/10.1021/ic500584a | *Inorg. Chem.* 2014, 53, 7294−7308

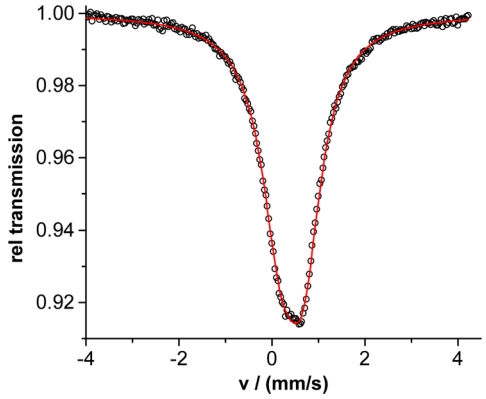

Figure 14. Mössbauer spectra of 7·$(MeCN)_4$ recorded at 80 K. The red line is a Lorentzian fit with parameters given in the text [line widths (fwhm) = 1.11 and 0.92 mm/s for the low- and high-energy lines of the doublet, respectively].

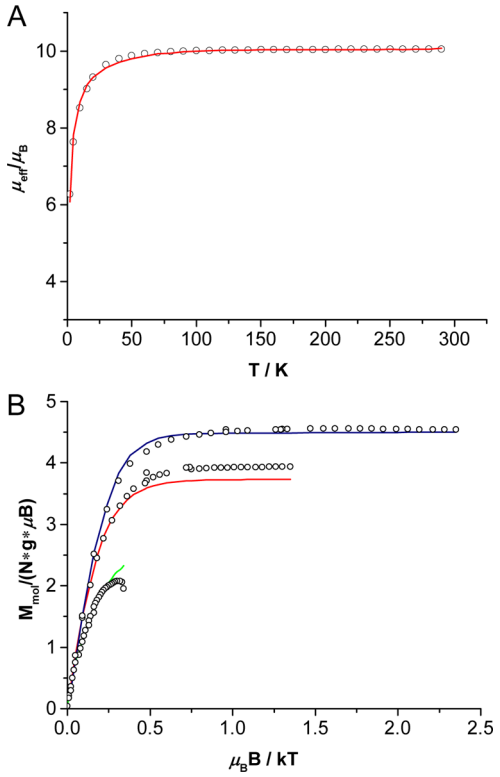

Figure 15. Temperature dependence of the effective magnetic moment of **1** (A) and of the magnetization, sampled at 1, 4, and 7 T on an inverse temperature scale (B). The lines represent a spin-Hamiltonian simulation for four spins S_i = 2 with single-ion zero-field splitting parameter D_i = −7.4 cm^{-1}, g_i = 2.05, and all six exchange coupling constants for the tetramer J_{ij} = −0.03 cm^{-1} (constrained to be equal).

reflections (*SHELXL-2013*).[69] All non-hydrogen atoms were refined anisotropically. Hydrogen atoms were introduced in their idealized positions and refined as riding atoms. A multiscan absorption correction[70] was applied for **1**·$(MeCN)_5$ and 7·$(MeCN)_4$, a numerical absorption correction[71] for **2**·(MeCN), and an empirical absorption correction for **3**·$(MeCN)_{0.25}$.

In the case of **3**·$(MeCN)_{0.25}$, several data collections have been performed. The crystal structure shows the following: (1) The heterocubane is heavily disordered: three of the four Me_3TACN ligands as well as their metal-connecting nitrogen atoms are disordered. We excluded a phase transition by collecting data at different temperatures: the static and dynamic disorder still persists with varying temperature.

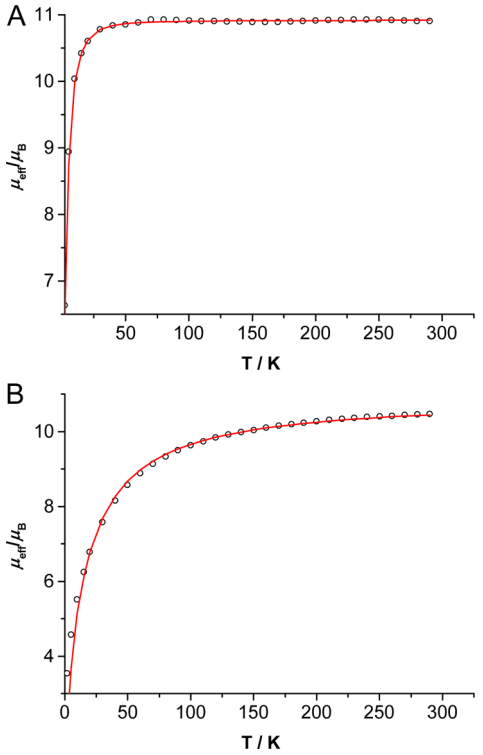

Figure 16. Temperature dependence of the effective magnetic moment of **3** (A) and **7** (B). The line in panel A represents a spin-Hamiltonian simulation with spin $S_1 = S_2 = {}^5/_2$, $S_3 = S_4 = 2$ with single-ion zero-field splitting parameter $D_1 = D_2 = 1$ cm^{-1}, $D_3 = D_4 = -8$ cm^{-1}, $g_i = 2.01$, and exchange coupling constants $J_{12} = J_{34} = -0.2$ cm^{-1} (between ions of the same valence), and $J_{13} = J_{14} = J_{23} = J_{24} = 0.1$ cm^{-1} (the mixed-valence pairs). The corresponding simulation for panel B has been made for four spins $S_i = {}^5/_2$ with $D_i = 1$ cm^{-1}, $g_i = 1.84$, and six exchange coupling constants $J_{ij} = -1.01$ cm^{-1}. (The low g values are physically meaningless and presumably result from the presence of a diamagnetic impurity.)

We measured data with Mo as well as with Cu radiation in order to detect a possible twinning (or other crystallographic problems). Our investigations showed neither a phase transition nor a twinning. The structure was solved and refined using a simple model in which all nonmetal atoms are isotropically refined. In parallel, with a considerable amount of resources, a convergent disorder model was also built. This model has double the number of parameters of the first one and 167 restraints. This model gives only modest improvement with respect to the reliability factors and residual electron density; therefore, we decided to publish the simplest model where all nonmetal atoms are isotropically refined. On request, we can provide the disordered model as well. (2) The unaccounted for residual electron density in large voids most probably corresponds to the solvent of crystallization (acetonitrile). A disorder model for this residual electron density could not be achieved. Therefore, a squeezed refinement has been performed.

Crystal and Molecular Structure Data. Table 5 contains the crystal data and experimental parameters for crystal structure analyses.

EPR Measurements. X-band EPR spectra were recorded on a ERS 300 spectrometer (ZWG/Magnettech GmbH, Berlin-Adlershof, Germany) equipped with a quartz Dewar for measurements at liquid-nitrogen temperature. g factors were calculated regarding a Cr^{3+}/MgO reference (g = 1.9796).

Mass Spectrometry. HR-ESI-MS spectra were collected using an Agilent Technologies 6210 time-of-flight liquid chromatography (LC)–MS instrument. Isotopic patterns were calculated using *mMass 5.5*.[72]

Electrospray ionization Fourier transform ion-cyclotron resonance (ESI-FTICR) MS/MS experiments were conducted with an Ionspec QFT-7 FTICR mass spectrometer (Agilent Technologies, Lake Forest, CA), equipped with a 7 T superconducting magnet and a Micromass Z-

dx.doi.org/10.1021/ic500584a | *Inorg. Chem.* 2014, 53, 7294−7308

Table 5. Crystal Data and Experimental Parameters for Crystal Structure Analyses

	1·$(MeCN)_5$	**2**·(MeCN)	**3**·$(MeCN)_{0.25}$	**7**·$(MeCN)_4$
formula	$C_{46}H_{99}Fe_4Mo_4N_{17}O_{16}$	$C_{62}H_{95}Fe_4Mo_4N_{21}O_{16}$	$C_{36.50}H_{84.75}F_{12}Fe_4Mo_4N_{11.25}O_{16}P_2$	$C_{46}H_{99}F_{24}Fe_4Mo_4N_{17}O_{16}P_4$
fw/(g/mol)	1753.58	1997.75	1834.51	2333.46
λ/Å	0.71073	0.71073	1.54178	0.71073
cryst syst	orthorhombic	triclinic	tetragonal	monoclinic
space group	$Pna2_1$	$P\bar{1}$	$P4/n$	$P2_1/c$
a/Å	25.3411(6)	13.4045(6)	30.6601(7)	17.9761(4)
b/Å	16.7869(4)	13.6116(6)	30.6601(7)	15.8643(3)
c/Å	16.1527(3)	24.2040(11)	15.3913(4)	29.1971(6)
α/deg	90	79.947(4)	90	90
β/deg	90	82.025(4)	90	93.683(2)
γ/deg	90	65.663(3)	90	90
V/Å^3	6871.3(3)	3951.0(3)	14468.5(6)	8309.2(3)
Z	4	2	8	4
density/(g/cm^3)	1.695	1.679	1.684	1.865
μ(Cu/Mo Kα)/mm^{-1}	1.595	1.4	12.954	1.458
F(000)	3576	2028	7364	4680
θ range/deg	3.23−29.22	4.60−26.00	2.87−68.42	2.16−26.84
reflns collected	58 663	50 275	111 587	71 090
indep reflns	18 000	15 370	13 287	17 367
completeness to θ/%	0.983	0.99	0.997	0.993
R(int)	0.0375	0.0928	0.0487	0.055
GoF on F^2	1.029	0.991	1.028	1
R1 [$I > 2\sigma(I)$]	0.0247	0.0535	0.0773	0.0368
wR2 [$I > 2\sigma(I)$]	0.054	0.1324	0.1816	0.0824
R1 (all data)	0.0302	0.0716	0.0847	0.0569
wR2 (all data)	0.067	0.1405	0.1867	0.0867
$\Delta\rho_{max}/\Delta\rho_{min}$/(e/Å^3)	0.72/−1.03	1.29/−1.39	2.39/−2.16	2.25/−1.28
CCDC	985330	985331	985332	985333

spray ESI source utilizing a stainless steel capillary with 0.65 mm inner diameter (Waters Co., Saint-Quentin, France).

The sample solutions (0.05−1.0 mM in 5:2 MeOH/MeCN) were introduced to the source with a syringe pump (Harvard Apparatus) at a flow rate of about 2.0 μL/min. Ionization parameters were set as follows: source temperature, 40 °C; temperature of desolvation gas, 40 °C; parameters for capillary (4200 V), sample cone (45 V), and extractor cone (10 V) voltages as well as the ion optics were optimized for maximum intensities. No nebulizer gas was used for the experiments. The ions were accumulated in the hexapole of the instrument for 2−10 s. Next, the ions were transferred to the FTICR analyzer cell by a quadrupole ion guide. The FTICR cell was operated at pressures below 1.0×10^{-9} mbar and detected by a standard excitation and detection sequence.

For tandem MS experiments, the ions of interest were mass-selected and subsequently vibrationally excited for the times indicated in the figures with a CO_2 laser in the IR region (IRMPD; 10.6 μm wavelength) to induce fragmentation.[73] The maximum laser power is 25 W and can be controlled by the instrument in increments of 25 W; the actual laser power used in each of the experiments is also given in the figures above. Multiple scans (up to 20) were averaged for each spectrum in order to improve the signal-to-noise ratio.

To conduct the ^{18}O exchange experiments in the gas phase, $H_2{}^{18}O$ was used as the reagent. The instrument hexapole cell (1.0×10^{-5} mbar) instead of the FTICR cell (pressures below 1.0×10^{-7} mbar) was used as the collision cell because of the higher pressure, giving rise to a higher exchange efficiency. The corresponding pulse program for H/D-exchange experiments was previously published.[74]

Materials. 1,4,7-Trimethyl-1,4,7-triazacyclononane (Me_3TACN),[75] $[Fe(MeCN)_2](OTf)_2$,[76] $ThPF_6$[77] and $(nBu_4N)_2[MoO_4]$[78] were prepared according to the literature procedures. DDQ was purchased from Sigma-Aldrich. TCNQ was purchased from ABCR, Germany. Iron(II) triflate $[Fe(OTf)_2]$ was obtained from Strem Chemicals. Water/^{18}O was obtained from Rotem Industries, Arava, Israel. Solvents were purified, dried, degassed, and stored over molecular sieves prior to use.

Synthesis of [[(Me_3TACN)Fe][μ-(MoO_4-κ^3O,O',O'')]]$_4$ (1). A total of 90 mg (0.53 mmol) of Me_3TACN was dissolved in 16 mL of acetonitrile, and 186 mg (0.53 mmol) of $Fe(OTf)_2$ was added. The suspension was stirred until all solid had dissolved, resulting in a clear slightly violet solution (30 min). Upon the addition of 339 mg (0.53 mmol) of $(nBu_4N)_2[MoO_4]$, the solution immediately became orange in color. Stirring was stopped immediately after complete addition of the molybdate to allow for precipitation of **1**·$(MeCN)_5$ as orange crystals, which were suitable for X-ray diffraction analysis. Prolonged drying under high vacuum afforded 173 mg (0.112 mmol, 85%) as an orange powder. Elem anal. Calcd for $C_{36}H_{84}Fe_4Mo_4N_{12}O_{16}$: C, 27.93; H, 5.47; N, 10.86. Found: C, 28.45; H, 5.54; N, 10.74. IR (KBr): $\tilde{\nu}$/cm^{-1} 2989 vw, 2964 w, 2944 w, 2873 m, 2853 m, 2828 w, 2811 m, 2776 w, 2718 vw, 1493 w, 1465 m, 1453 m, 1423 vw, 1385 vw, 1364 vw, 1300 w, 1258 vw, 1216 vw, 1157 w, 1132 vw, 1091 w, 1066 m, 1020 s, 909 m, 849 vs, 768 s, 572 w, 430 vw. ^1H NMR (CD_2Cl_2, 293 K): δ 101.8 (6H, $\Delta\nu_{1/2}$ = 290 Hz), 42.4 (9H, $\Delta\nu_{1/2}$ = 180 Hz), 40.5 (6H, $\Delta\nu_{1/2}$ = 630 Hz). HR-ESI-MS. Calcd for $[C_{36}H_{84}Fe_4Mo_4N_{12}O_{16}]^+$: m/z 1547.977. Found: m/z 1547.974.

Synthesis of [[(Me_3TACN)Fe][μ-(MoO_4-κ^3O,O',O'')]]$_4$($TCNQ$)$_2$ (2). A total of 200 mg (0.129 mmol) was suspended in 100 mL of acetonitrile and treated with 52.8 mg of TCNQ (0.259 mmol, 2 equiv). The resulting deep-green solution was stirred at room temperature overnight, followed by removal of all volatiles under high vacuum. Fresh acetonitrile was added, and the resulting solution was layered with 200 mL of diethyl ether to give blue crystals of **2** (MeCN), which were suitable for single-crystal X-ray diffraction analysis. Prolonged drying under high vacuum afforded 178 mg (0.091 mmol, 70%) of **2** as a greenish powder. Elem anal. Calcd for $C_{60}H_{92}Fe_4Mo_4N_{20}O_{16}$: C, 36.83; H, 4.74; N, 14.32. Found: C, 37.18; H, 4.88; N, 14.29. IR (KBr): $\tilde{\nu}$/cm^{-1} 2991 vw, 2969 vw, 2899 w, 2867 w, 2818 vw, 2177 vs, 2151 s, 1586 w, 1503 s, 1464 m, 1424 w, 1384 w, 1360 s, 1298 w, 1260 vw, 1208 vw, 1179 w, 1156 w, 1129 vw, 1108 vw, 1083 w, 1073 w, 1060 m, 1014 m, 1010 m, 933 w, 866 vs, 824 s, 775 vs, 577 w, 540 vw, 480 w, 445 w, 418 vw, 406 vw.

dx.doi.org/10.1021/ic500584a | Inorg. Chem. 2014, 53, 7294−7308

Synthesis of [[(Me$_3$TACN)Fe][μ-(MoO$_4$-κ^3*O,O′,O″*)]]$_4$(PF$_6$)$_2$ (3). A total of 500 mg (0.323 mmol) of **1** was suspended in 100 mL of acetonitrile and stirred overnight. A total of 132 mg of TCNQ (0.646 mmol) was then added, resulting in an immediate color change to a brown suspension. Stirring was continued for another 48 h to allow for completion of the reaction. To the resulting green solution was added 250 mg (0.645 mmol) of [*n*Bu$_4$N](PF$_6$), and the solution was concentrated to 50 mL. Crude **3** was crashed by the addition of diethyl ether, and the suspension was filtered off (three times). The isolated solid was redissolved in 50 mL of acetonitrile, and the resulting solution was layered with diethyl ether, resulting in precipitation of 199 mg (0.108 mmol, 34%) of **3**·(MeCN)$_{0.25}$ in the form of brown crystals. Drying under high vacuum afforded a brown powder of **3**. Elem anal. Calcd for $C_{36}H_{84}F_{12}Fe_4Mo_4N_{12}O_{16}P_2$: C, 23.52; H, 4.61; N, 9.14. Found: C, 23.79; H, 4.54; N, 8.80. IR (KBr): $\tilde{\nu}$/cm^{-1} 2995 vw, 2969 vw, 2901 w, 2869 w, 2822 vw, 2781 vw, 2723 vw, 1498 vw, 1466 m, 1453 w, 1425 vw, 1383 vw, 1364 vw, 1300 w, 1261 vw, 1212 vw, 1157 vw, 1130 vw, 1113 vw, 1084 w, 1074 w, 1061 m, 1015 m, 989 w, 937 w, 869 vs, 840 vs, 776 s, 578 vw, 557 m, 2498 vw, 445 vw, 419 vw. HR-ESI-MS. Calcd for $[C_{36}H_{84}Fe_4Mo_4N_{12}O_{16}]^+$: *m*/*z* 773.988. Found: *m*/*z* 773.985.

Synthesis of [[(Me$_3$TACN)Fe]$_4$[μ-([MoO$_4$]$_3$[MoO$_4$(MeCN-κ*N*)])-κ^3*O,O′,O″*)](PF$_6$)$_4$ (7). A total of 54.1 mg (0.0349 mmol) of **1** was suspended in 100 mL of acetonitrile overnight and subsequently treated with 63.1 mg (0.174 mmol, 5 equiv) of ThPF$_6$. This was accompanied by an immediate color change to give a brown suspension and finally a yellow solution. All volatiles were then removed under reduced pressure. The crude product was redissolved in 10 mL of acetonitrile and precipitated by the addition of 100 mL of diethyl ether. The mixture was filtered off using a stainless steel filter cannula. Redissolving the solid residue in 2 mL of acetonitrile and layering of the resulting solution with diethyl ether afforded **7**·(MeCN)$_4$ as orange single crystals, which were suitable for X-ray diffraction analysis. Prolonged drying under high vacuum removed the cocrystallized solvent to yield **7** as an orange powder; the coordinating acetonitrile is not removed by this procedure. Elem anal. Calcd for $C_{38}H_{87}F_{24}Fe_4Mo_4N_{13}O_{16}P_4$: C, 21.04; H, 4.04; N, 8.39. Found: C, 21.30; H, 4.20; N, 8.23. IR (KBr): $\tilde{\nu}$/cm^{-1} 2984 vw, 2961 vw, 2928 vw, 2911 vw, 2878 vw, 2829 vw, 2250 vw, 1653 vw, 1497 vw, 1466 w, 1457 w, 1384 vw, 1363 vw, 1298 vw, 1262 vw, 1205 vw, 1157 w, 1126 w, 1104 w, 1096 w, 1069 w, 1058 w, 1007 m, 987 w, 960 w, 871 vs, 840 vs, 778 vs, 746 w, 736 w, 706 vw, 625 vw, 581 vw, 575 vw, 557 m, 493 vw, 480 vw, 449 w, 419 w.

■ ASSOCIATED CONTENT

Ⓢ Supporting Information

X-ray crystallographic data in CIF format, depiction of the molecular structure of **3**·(MeCN)$_{0.25}$, crystallographic Information on TCNQ and related compounds, mass spectra of **1**, Mössbauer spectra of **7**·(MeCN)$_4$ at 160 and 240 K, and IR spectra of the crystallized compounds. This material is available free of charge via the Internet at http://pubs.acs.org.

■ AUTHOR INFORMATION

Corresponding Author

*E-mail: christian.limberg@chemie.hu-berlin.de. Tel: +49 30 2093 7382. Fax: +49 30 2093 6966.

Notes

The authors declare no competing financial interest.

■ ACKNOWLEDGMENTS

We thank Prof. Dr. Christoph Schalley for helpful discussions and Marie Luise Wind for help with some of the practical work and analysis. We are grateful to the Cluster of Excellence "Unifying Concepts in Catalysis", funded by the Deutsche Forschungsgemeinschaft, and the Humboldt-Universität zu Berlin for financial support.

■ DEDICATION

Dedicated to Professor Robert Schlögl on occasion of his 60th birthday.

■ REFERENCES

(1) Roggan, S.; Limberg, C.; Brandt, M.; Ziemer, B. *J. Organomet. Chem.* **2005**, *690*, 5282−5289.
(2) Roggan, S.; Limberg, C.; Ziemer, B. *Angew. Chem., Int. Ed.* **2005**, *44*, 5259−5262.
(3) Roggan, S.; Limberg, C.; Ziemer, B.; Siemons, M.; Simon, U. *Inorg. Chem.* **2006**, *45*, 9020−9031.
(4) Roggan, S.; Limberg, C. *Inorg. Chim. Acta* **2006**, *359*, 4698−4722.
(5) Knispel, C.; Limberg, C.; Mehring, M. *Organometallics* **2009**, *28*, 646−651.
(6) Knispel, C.; Limberg, C. *Organometallics* **2011**, *30*, 3701−3703.
(7) Mekala, R.; Supriya, S.; Das, S. K. *Inorg. Chem.* **2013**, *52*, 9708−9710.
(8) Dong, X.; Zhang, Y.; Liu, B.; Zhen, Y.; Hu, H.; Xue, G. *Inorg. Chem.* **2012**, *51*, 2318−2324.
(9) Zhen, Y.; Liu, B.; Li, L.; Wang, D.; Ma, Y.; Hu, H.; Gao, S.; Xue, G. *Dalton Trans.* **2012**, *42*, 58−62.
(10) Liu, B.; Li, L.; Zhang, Y.; Ma, Y.; Hu, H.; Xue, G. *Inorg. Chem.* **2011**, *50*, 9172−9177.
(11) Long, D.-L.; Kögerler, P.; Farrugia, L. J.; Cronin, L. *Dalton Trans.* **2005**, 1372−1380.
(12) Müller, A.; Das, S. K.; Krickemeyer, E.; Kögerler, P.; Bögge, H.; Schmidtmann, M. *Solid State Sci.* **2000**, *2*, 847−854.
(13) Xu, L.; Li, Z.; Liu, H.; Huang, J.; Zhang, Q. *Chem.—Eur. J.* **1997**, *3*, 226−231.
(14) Niu, J.-Y.; Wang, J.-P.; You, X.-Z.; Mak, T. C. W.; Zhou, Z.-Y. *Polyhedron* **1996**, *15*, 3963−3969.
(15) Niu, J.-Y.; You, X.-Z.; Wang, J.-P. *Transition Met. Chem.* **1996**, *21*, 38−42.
(16) Zhao, J.; Liu, J.; Wang, J.; Niu, J.-Y. *Chem. Lett.* **2009**, *38*, 474−475.
(17) Long, D.-L.; Kögerler, P.; Farrugia, L. J.; Cronin, L. *Chem.—Asian J.* **2006**, *1*, 352−357.
(18) Zapf, P. J.; Hammond, R. P.; Haushalter, R. C.; Zubieta, J. *Chem. Mater.* **1998**, *10*, 1366−1373.
(19) Chen, H.-L.; Li, M.-X.; He, X.; Wang, Z.-X.; Shao, M.; Zhu, S.-R. *Inorg. Chim. Acta* **2010**, *363*, 3186−3193.
(20) Zhang, X.-M.; Fang, R.-Q.; Ng, S. W. *Acta Crystallogr., Sect. E: Struct. Rep. Online* **2004**, *60*, m1049−m1050.
(21) Huang, S. D.; Shan, Y. *J. Solid State Chem.* **2000**, *152*, 229−235.
(22) Hagrman, P. J.; Zubieta, J. *Inorg. Chem.* **2000**, *39*, 5218−5224.
(23) Chaudhuri, P.; Wieghardt, K.; Nuber, B.; Weiss, J. *J. Chem. Soc., Chem. Commun.* **1987**, 1198−1199.
(24) Lettko, K.; Liu, S.; Zubieta, J. *Acta Crystallogr., Sect. C: Cryst. Struct. Commun.* **1991**, *47*, 1723−1725.
(25) Holz, R. C.; Elgren, T. E.; Pearce, L. L.; Zhang, J. H.; O'Connor, C. J.; Que, L. J. *Inorg. Chem.* **1993**, *32*, 5844−5850.
(26) Davydov, R. M.; Smieja, J.; Dikanov, S. A.; Zang, Y.; Que, L. J.; Bowman, M. K. *J. Biol. Inorg. Chem.* **1999**, *4*, 292−301.
(27) Lu, J.; Lü, C.-H.; Yu, J.-H.; Xu, J.-Q.; Li, Y.; Zhang, X.; Wang, T.-G.; Yang, Q.-X. *Polyhedron* **2004**, *23*, 755−761.
(28) Lü, C.-H.; Xu, J.-Q.; Yu, J.-H.; Ye, L.; Li, Y.; Lu, J.; Wang, T.-G.; Cao, J.-X. *Mendeleev Commun.* **2003**, *13*, 167−168.
(29) Falkenhagen, J. P.; Limberg, C.; Demeshko, S.; Horn, S.; Haumann, M.; Braun, B.; Mebs, S. *Dalton Trans.* **2014**, *43*, 806−816.
(30) Blakesley, D. W.; Payne, S. C.; Hagen, K. S. *Inorg. Chem.* **2000**, *39*, 1979−1989.
(31) Holm, R. H.; Hawkins, C. J. In *NMR of paramagnetic molecules*; La Mar, G. N., Horrocks, W. D. J., Holm, R. H., Eds.; Academic Press: New York, 1973; pp 243−332.
(32) Connelly, N. G.; Geiger, W. E. *Chem. Rev.* **1996**, *96*, 877−910.
(33) Batsanov, S. S. *Inorg. Mater.* **2001**, *37*, 871−885.
(34) Huang, J.; Kingsbury, S.; Kertesz, M. *Phys. Chem. Chem. Phys.* **2008**, *10*, 2625−2635.

(35) Miller, J. S.; Zhang, J. H.; Reiff, W. M.; Dixon, D. A.; Preston, L. D.; Reis, A. H.; Gebert, E.; Extine, M.; Troup, J. *J. Phys. Chem.* **1987**, *91*, 4344−4360.
(36) Khatkale, M. S.; Devlin, J. P. *J. Chem. Phys.* **1979**, *70*, 1851−1859.
(37) Long, R. E.; Sparks, R. A.; Trueblood, K. N. *Acta Crystallogr.* **1965**, *18*, 932−939.
(38) Hoekstra, A.; Spoelder, T.; Vos, A. *Acta Crystallogr., Sect. B: Struct. Crystallogr. Cryst. Chem.* **1972**, *28*, 14−25.
(39) Kistenmacher, T. J.; Emge, T. J.; Bloch, A. N.; Cowan, D. O. *Acta Crystallogr., Sect. B: Struct. Crystallogr. Cryst. Chem.* **1982**, *38*, 1193−1199.
(40) Melby, L. R.; Harder, R. J.; Hertler, W. R.; Mahler, W.; Benson, R. E.; Mochel, W. E. *J. Am. Chem. Soc.* **1962**, *84*, 3374−3387.
(41) Bozio, R.; Girlando, A.; Pecile, C. *J. Chem. Soc., Faraday Trans. 2* **1975**, *71*, 1237−1254.
(42) Baumann, F.; Kaim, W.; Olabe, J. A.; Parise, A. R.; Jordanov, J. *J. Chem. Soc., Dalton Trans.* **1997**, 4455−4460.
(43) Bandrauk, A. D.; Truong, K. D.; Carlone, C.; Jandl, S.; Ishii, K. *J. Phys. Chem.* **1985**, *89*, 434−442.
(44) Gundel, D.; Sixl, H.; Metzger, R. M.; Heimer, N. E.; Harms, R. H.; Keller, H. J.; Nöthe, D.; Wehe, D. *J. Chem. Phys.* **1983**, *79*, 3678−3688.
(45) Miller, J. S.; Calabrese, J. C.; Harlow, R. L.; Dixon, D. A.; Zhang, J. H.; Reiff, W. M.; Chittipeddi, S. R.; Selover, M. A.; Epstein, A. J. *J. Am. Chem. Soc.* **1990**, *112*, 5496−5506.
(46) Lü, J.-M.; Rosokha, S. V.; Kochi, J. K. *J. Am. Chem. Soc.* **2003**, *125*, 12161−12171.
(47) Miller, J. S.; Krusic, P. J.; Dixon, D. A.; Reiff, W. M.; Zhang, J. H.; Anderson, E. C.; Epstein, A. J. *J. Am. Chem. Soc.* **1986**, *108*, 4459−4466.
(48) Addison, A. W.; Rao, T. N.; Reedijk, J.; van Rijn, J.; Verschoor, G. C. *J. Chem. Soc., Dalton Trans.* **1984**, 1349−1356.
(49) Brown, C. A.; Remar, G. J.; Musselman, R. L.; Solomon, E. I. *Inorg. Chem.* **1995**, *34*, 688−717.
(50) Snodin, M. D.; Ould-Moussa, L.; Wallmann, U.; Lecomte, S.; Bachler, V.; Bill, E.; Hummel, H.; Weyhermüller, T.; Hildebrandt, P.; Wieghardt, K. *Chem.—Eur. J.* **1999**, *5*, 2554−2565.
(51) Cruywagen, J. J.; Heyns, J. B. B. *Inorg. Chem.* **1987**, *26*, 2569−2572.
(52) Bossek, U.; Nühlen, D.; Bill, E.; Glaser, T.; Krebs, C.; Weyhermüller, T.; Wieghardt, K.; Lengen, M.; Trautwein, A. X. *Inorg. Chem.* **1997**, *36*, 2834−2843.
(53) Gütlich, P.; Bill, E.; Trautwein, A. X. *Mössbauer Spectroscopy and Transition Metal Chemistry: Fundamentals and Applications*; Springer Verlag: Berlin, 2011.
(54) Hotzelmann, R.; Wieghardt, K.; Ensling, J.; Romstedt, H.; Guetlich, P.; Bill, E.; Floerke, U.; Haupt, H.-J. *J. Am. Chem. Soc.* **1992**, *114*, 9470−9483.
(55) Trifirò, F.; Notarbartolo, S.; Pasquon, I. *J. Catal.* **1971**, *22*, 324−332.
(56) Allison, J. N.; Goddard, W. A., III. *J. Catal.* **1985**, *92*, 127−135.
(57) Chung, J. S.; Miranda, R.; Bennett, C. O. *J. Catal.* **1988**, *114*, 398−410.
(58) Yamada, H.; Niwa, M.; Murakami, Y. *Appl. Catal., A* **1993**, *96*, 113−123.
(59) O'Brien, M. G.; Beale, A. M.; Jacques, S. D. M.; Buslaps, T.; Honkimaki, V.; Weckhuysen, B. M. *J. Phys. Chem. C* **2009**, *113*, 4890−4897.
(60) Huang, Y.; Cong, L.; Yu, J.; Eloy, P.; Ruiz, P. *J. Mol. Catal. A: Chem.* **2009**, *302*, 48−53.
(61) Beale, A. M.; Jacques, S. D. M.; Sacaliuc-Parvalescu, E.; O'Brien, M. G.; Barnes, P.; Weckhuysen, B. M. *Appl. Catal., A* **2009**, *363*, 143−152.
(62) Routray, K.; Zhou, W.; Kiely, C. J.; Grünert, W.; Wachs, I. E. *J. Catal.* **2010**, *275*, 84−98.
(63) Fievez, T.; Geerlings, P.; Weckhuysen, B. M.; Proft, F. d. *ChemPhysChem* **2011**, *12*, 3281−3290.
(64) Uhlrich, J. J.; Sainio, J.; Lei, Y.; Edwards, D.; Davies, R.; Bowker, M.; Shaikhutdinov, S.; Freund, H.-J. *Surf. Sci.* **2011**, *605*, 1550−1555.
(65) Bamroongwongdee, C.; Bowker, M.; Carley, A. F.; Davies, P. R.; Davies, R. J.; Edwards, D. *Faraday Discuss.* **2013**, *162*, 201−212.
(66) Bowker, M.; Holroyd, R.; House, M. P.; Bracey, R.; Bamroongwongdee, C.; Shannon, M.; Carley, A. F. *Top. Catal.* **2008**, *48*, 158−165.
(67) Reuss, G.; Disteldorf, W.; Gamer, A. O.; Hilt, A. *Ullmann's Encyclopedia of Industrial Chemistry*; Wiley-VCH Verlag GmbH & Co. KGaA: Weinheim, Germany, 2005.
(68) Machiels, C. J.; Chowdhry, U.; Sleight, A. W. Molybdate and Tungstate Catalysts for Methanol Oxidation. *Symposium on the Role of Solid State Chemistry in Catalysis*; Division of Petroleum Chemistry, American Chemical Society: Washington, DC, 1983.
(69) Sheldrick, G. M. *Acta Crystallogr., Sect. A: Found. Crystallogr.* **2008**, *64*, 112−122.
(70) Spek, A. L. *J. Appl. Crystallogr.* **2003**, *36*, 7−13.
(71) *STOE X-RED*; Stoe & Cie: Darmstadt, Germany, 1991.
(72) Strohalm, M.; Kavan, D.; Novák, P.; Volný, M.; Havlíček, V. *Anal. Chem.* **2010**, *82*, 4648−4651.
(73) Sattler, D.; Schlesinger, M.; Mehring, M.; Schalley, C. A. *ChemPlusChem* **2013**, *78*, 1005−1014.
(74) Weimann, D. P.; Winkler, H. D. F.; Falenski, J. A.; Koksch, B.; Schalley, C. A. *Nat. Chem.* **2009**, *1*, 573−577.
(75) Schoenfeldt, N. J.; Korinda, A. W.; Notestein, J. M. *Chem. Commun.* **2010**, *46*, 1640−1642.
(76) Heintz, R. A.; Smith, J. A.; Szalay, P. S.; Weisgerber, A.; Dunbar, K. R. *Inorg. Synth.* **2002**, *33*, 75−83.
(77) Lee, W. K.; Liu, B.; Park, C. W.; Shine, H. J.; Whitmire, K. H. *J. Org. Chem.* **1999**, *64*, 9206−9210.
(78) Klemperer, W. G.; Liu, R. S. *Inorg. Chem.* **1980**, *19*, 3863−3864.